

GROWTH OF OPTOELECTRONIC DEVICE-QUALITY
 $\text{In}_{0.4}\text{Ga}_{0.6}\text{As}$ ON GaAs BY MOLECULAR BEAM EPITAXY

BY

PAULO ROBERTO FOGAÇA RIBAS

A DISSERTATION PRESENTED TO THE GRADUATE SCHOOL
OF THE UNIVERSITY OF FLORIDA IN PARTIAL FULFILLMENT
OF THE REQUIREMENTS FOR THE DEGREE OF
DOCTOR OF PHILOSOPHY

UNIVERSITY OF FLORIDA

1990
- - -

To my wife, Marcia, and children,
Rafael, Gabriel, Renato, and Priscilla

ACKNOWLEDGMENTS

I would like to express my gratitude to my supervisor, Dr. R. M. Park, for his continuous direction and support during the course of my doctoral research. His valuable input contributed significantly to the progress of my work.

I wish to acknowledge the support of Dr. P. H. Holloway, Dr. R. E. Hummel, Dr. K. S. Jones, and Dr. S. S. Li, members of my supervisory committee. Special thanks are due to Dr. Li and his team who prepared the $\text{In}_{0.4}\text{Ga}_{0.6}\text{As}$ PIN photodetector devices discussed in Chapter 5 of this work.

I wish to express my gratitude to the Brazilian Army for providing the opportunity and the necessary financial support for the pursuit of my doctoral degree. I also acknowledge the support of the National Council for Scientific and Technological Development of Brazil (Conselho Nacional de Desenvolvimento Científico e Tecnológico--CNPq/Brasil).

I would like to thank Dr. Uptal Das for performing the photoluminescence analysis of high indium content $\text{In}_x\text{Ga}_{1-x}\text{As}$ material and Dr. T. Anderson for permission to use his Hall-effect equipment.

I wish to acknowledge Drs. A. Miller and P. LiKamWa, of CREOL, University of Central Florida, for their help and valuable discussions associated with photoluminescence and

absorption analysis performed during my extended visit to CREOL.

Special thanks are owed to V. Krishnamoorthy for TEM analyses performed on the $\text{In}_x\text{Ga}_{1-x}\text{As}/\text{GaAs}$ heterostructures.

I would like to acknowledge Prof. Y. W. Lin, M. M. Puga, W. Acree, A. Hoelzer, C. Rouleau, M. J. Tropher, B. Pathangey, M. Ogawa, and K. Truman, for helping me during the experimental work.

Finally, I would like to thank my wife, Marcia, and children, Rafael, Gabriel, Renato, and Priscilla, for their continuous support, understanding, and encouragement.

TABLE OF CONTENTS

	<u>page</u>
ACKNOWLEDGEMENTS.....	iii
LIST OF TABLES.....	vii
LIST OF FIGURES.....	ix
ABSTRACT.....	xii
 CHAPTERS	
1 INTRODUCTION.....	1
Motivation and Objectives.....	1
Literature Survey.....	3
Introduction.....	3
Strained-Layer Superlattices.....	4
Strain Relief Mechanisms.....	5
Strain-Induced Modifications of Semiconductor Properties.....	12
Utilization of Modified Properties Created by Strain.....	13
In _x Ga _{1-x} As Growth by MBE.....	14
Scope of Present Work.....	18
2 MOLECULAR BEAM EPITAXY: SYSTEM CONFIGURATION AND CALIBRATION.....	20
Introduction.....	20
Varian GEN II MBE System Configuration.....	21
Set-up of the MBE System.....	28
Substrate Temperature Calibration.....	28
Effusion Source Preparation Procedures.....	30
Substrate and Source Materials Specification...	33
Growth System Calibration.....	34
Theory.....	35
Flux Calibration.....	41
3 GROWTH AND ELECTRICAL CHARACTERIZATION OF GaAs AND AlGaAs EPITAXIAL LAYERS.....	49
Substrate Preparation Procedures.....	49

Growth and Electrical Characterization of GaAs Epilayers.....	54
Growth and Characterization of AlGaAs Epitaxial Layers.....	62
Conclusions.....	73
4 GROWTH AND CHARACTERIZATION OF $\text{In}_x\text{Ga}_{1-x}\text{As}/\text{GaAs}$ HETEROSTRUCTURES.....	74
Composition Analysis.....	75
Determination of Residual Strain in $\text{In}_x\text{Ga}_{1-x}\text{As}/\text{GaAs}$ Layers.....	79
Identification of Strain Relief Mechanisms.....	86
Photoluminescence and Absorption Analysis of $\text{In}_x\text{Ga}_{1-x}\text{As}/\text{GaAs}$ Layers.....	94
Conclusions.....	98
5 GROWTH OF OPTOELECTRONIC DEVICE-QUALITY $\text{In}_x\text{Ga}_{1-x}\text{As}$	101
Introduction.....	101
Growth of High In Content $\text{In}_x\text{Ga}_{1-x}\text{As}$ Layers.....	102
Device-Quality $\text{In}_{0.4}\text{Ga}_{0.6}\text{As}$ Grown on GaAs.....	112
$\text{In}_{0.4}\text{Ga}_{0.6}\text{As}$ p-i-n Photodetector Fabrication.....	134
Conclusions.....	138
6 CONCLUSIONS AND RECOMMENDATIONS.....	140
REFERENCES.....	144
BIOGRAPHICAL SKETCH.....	148

LIST OF TABLES

Table	Page
2.1 Correspondence between monitored temperature (T_{mon}) and actual temperature (T_{ss}).....	30
2.2 Temperature of each furnace during degassing of the source materials after a system bake-out....	32
2.3 Specification of the GaAs substrates.....	33
2.4 Specification of the source materials used in the MBE system.....	34
2.5 Gallium beam equivalent pressure (BEP) as a function of furnace temperature.....	42
2.6 Aluminum beam equivalent pressure as a function Al furnace temperature.....	44
2.7 Indium beam equivalent pressure as a function In furnace temperature.....	45
2.8 Arsenic beam equivalent pressure as a function of As furnace temperature.....	47
3.1 Electronic properties of Si-doped GaAs layers...	57
3.2 Electronic properties of Be-doped GaAs layers...	58
3.3 Electronic properties of Si-doped GaAs layers as a function of substrate temperature during growth.....	62
3.4 Growth parameters, room temperature band gap, and x values for a series of $\text{Al}_x\text{Ga}_{1-x}\text{As}$ layers....	65
3.5 Electronic properties of Si-doped and Be-doped $\text{Al}_x\text{Ga}_{1-x}\text{As}$ layers grown by MBE.....	69
4.1 Growth conditions for $\text{In}_x\text{Ga}_{1-x}\text{As}$ epitaxial layers grown on GaAs substrates.....	75

4.2	Lattice parameter, (400) interplanar distance, and angle of the corresponding X-ray beam for binary compounds.....	80
4.3	Lattice parameters and residual strain of $\text{In}_x\text{Ga}_{1-x}\text{As}$ layers grown on GaAs substrates.....	83
4.4	Conditions during growth of low and high indium content $\text{In}_x\text{Ga}_{1-x}\text{As}$ single layers.....	86
4.5	Photoluminescence and absorption data obtained from $\text{In}_x\text{Ga}_{1-x}\text{As}/\text{GaAs}$ layers, where the In content was measured by electron microprobe.....	95
4.6	Absorption data obtained from $\text{In}_x\text{Ga}_{1-x}\text{As}/\text{GaAs}$ layers, where the In content was measured by electron microprobe.....	97
5.1	Growth parameters of two structures comprised of an InGaAs thick layer grown on an InGaAs/InAlAs SLS. In sample 037 the InGaAs buffer was not grown.....	104
5.2	Experimental data of thick $\text{In}_x\text{Ga}_{1-x}\text{As}$ layers grown on GaAs.....	119
5.3	Experimental data obtained from thick $\text{In}_x\text{Ga}_{1-x}\text{As}$ epitaxial layers grown on a multi-stage strain-relief buffer.....	127
5.4	Electronic properties of doped $\text{In}_{0.4}\text{Ga}_{0.6}\text{As}$ layers obtained by Hall-effect measurements at room temperature.....	135

LIST OF FIGURES

Figure	Page
1.1 Critical thickness (h_c) versus In content (x) for $\text{In}_x\text{Ga}_{1-x}\text{As}$. The points represent some experimental results (figure from Nakao and Yao [23]).....	11
2.1 Schematic diagram of the Varian GEN II MBE growth chamber configuration.....	24
2.2 Beam equivalent pressure of metals versus furnace temperature.....	46
2.3 Arsenic beam equivalent pressure as a function of As furnace temperature.....	48
3.1 Substrate orientation during RHEED pattern observation.....	52
3.2 Carrier concentration of GaAs layers as a function of dopant furnace temperature.....	59
3.3 Room temperature carrier mobility as a function of carrier concentration in n-type and p-type GaAs layers.....	60
3.4 Electron mobilities in Si-doped GaAs as a function of substrate temperature (carrier concentration $\approx 2 \times 10^{16} \text{ cm}^{-3}$).....	61
3.5 AlGaAs/GaAs structures grown by MBE for electrical measurements.....	67
3.6 Electron concentration of Si-doped $\text{Al}_x\text{Ga}_{1-x}\text{As}$ layers as a function of silicon source temperature for two values of x , namely 0.2 and 0.3.....	71
3.7 Carrier concentration of Be-doped $\text{Al}_x\text{Ga}_{1-x}\text{As}$ layers as a function of beryllium source temperature for two values of x , namely 0.2 and 0.3.....	72
4.1 Major crystallographic planes and directions in a cubic lattice.....	81

4.2	X-ray diffraction patterns observed for 1 μm thick InGaAs epilayers grown on GaAs substrates...	84
4.3	X-ray diffraction patterns observed for 1 μm thick InGaAs epilayers grown on GaAs substrates...	85
4.4	InGaAs/GaAs interface showing absence of dislocations in the InGaAs layer and dislocations generated at the interface.....	88
4.5	GaAs buffer layer in a InGaAs/GaAs hetero-structure presenting dislocations generated and propagated from the interface ($x = 0.12$).....	89
4.6	InGaAs layer ($x \approx 0.2$) showing dislocations originated from both the InGaAs/GaAs interface and growth surface.....	90
4.7	$\text{In}_{0.5}\text{Ga}_{0.5}\text{As}$ epilayer grown on GaAs, presenting a high dislocation density originated mostly at the free surface.....	91
4.8	Thick $\text{In}_{0.5}\text{Ga}_{0.5}\text{As}$ layer showing some dislocations nucleated at the free surface and propagating through the epilayer ($x \approx 0.2$).....	92
4.9	Absorption spectra of an $\text{In}_{0.05}\text{Ga}_{0.95}\text{As}$ layer. The second edge at left ($\approx 895 \text{ nm}$) corresponds to GaAs substrate absorption.....	96
5.1	X-TEM micrographs of a structure composed of a 1.0 μm thick indium content InGaAs layer grown on matched InGaAs/InAlAs SLS and InGaAs buffer layer showing (a) the whole structure and (b) a highly distorted SLS region.....	105
5.2	X-TEM micrograph of the top $\text{In}_{0.5}\text{Ga}_{0.5}\text{As}$ layer grown on a matched InGaAs/InAlAs SLS and InGaAs buffer layer.....	106
5.3	X-TEM micrographs of a structure with two InGaAs/InAlAs SLSs and an InGaAs layer grown between them: (a) the two SLSs and intermediate InGaAs layer; (b) top InGaAs layer showing a reduced dislocation density.....	108
5.4	X-TEM micrographs of a 1.0 μm thick $\text{In}_{0.5}\text{Ga}_{0.5}\text{As}$ layer grown on different SLSs: (a) $\text{In}_{0.35}\text{Ga}_{0.65}\text{As}/\text{In}_{0.65}\text{Al}_{0.35}\text{As}$ SLS; (b) InAs/GaAs SLS.....	110

5.5	X-TEM micrographs of a sample showing the interface between the SLS and the GaAs buffer layer. No dislocations are observed in the buffer layer.....	111
5.6	Schematic diagram of a "multi-stage" strain-relief buffer system grown by MBE in order to realize device-quality $\text{In}_{0.4}\text{Ga}_{0.6}\text{As}$ epilayers on GaAs.....	114
5.7	X-TEM micrographs illustrating (a) heavily dislocated $\text{In}_{0.4}\text{Ga}_{0.6}\text{As}$ grown directly on GaAs and (b) nearly dislocation-free $\text{In}_{0.4}\text{Ga}_{0.6}\text{As}$	116
5.8	X-TEM micrograph composite of the complete "multi-stage" buffer system illustrating the strained-layer superlattice.....	118
5.9	Schematic diagram of a "multi-stage" strain-relief system with a slightly different SLS design.....	125
5.10	Planar TEM micrographs of two samples presenting dislocation densities equal to (a) $\approx 10^8 \text{ cm}^{-2}$ and (b) $\approx 2 \times 10^6 \text{ cm}^{-2}$, respectively.....	128
5.11	Typical 13K photoluminescence spectrum recorded from a 3 μm thick buffered $\text{In}_{0.4}\text{Ga}_{0.6}\text{As}$ epitaxial layer grown on GaAs.....	129
5.12	Dislocation density versus electron mobility in buffered $\text{In}_{0.4}\text{Ga}_{0.6}\text{As}$ epitaxial layers grown on GaAs.....	132
5.13	Dislocation density as a function of effective strain in buffered $\text{In}_{0.4}\text{Ga}_{0.6}\text{As}$ epitaxial layers grown on GaAs.....	133
5.14	Schematic diagram of an $\text{In}_{0.4}\text{Ga}_{0.6}\text{As}$ p-i-n photodiode showing the cross-section view of the device.....	136
5.15	Spectral response of an $\text{In}_{0.4}\text{Ga}_{0.6}\text{As}$ p-i-n photodiode prepared on a GaAs substrate.....	137

Abstract of Dissertation Presented to the Graduate School
of the University of Florida in Partial Fulfillment of the
Requirements for the Degree of Doctor of Philosophy

GROWTH OF OPTOELECTRONIC DEVICE-QUALITY
 $\text{In}_{0.4}\text{Ga}_{0.6}\text{As}$ ON GaAs BY MOLECULAR BEAM EPITAXY

By

Paulo Roberto Fogaça Ribas

August, 1990

Chairman: Dr. Robert M. Park
Major Department: Materials Science and Engineering

The present investigation develops a novel approach to growing optoelectronic device-quality $\text{In}_{0.4}\text{Ga}_{0.6}\text{As}$ epitaxial layers on GaAs substrates employing the molecular beam epitaxy technique. Experimental work was performed in a Varian GEN II MBE system configured with sources for Ga, Al, In, Be (p-type dopant), Si (n-type dopant), and As_2 .

Growth and characterization of $\text{In}_x\text{Ga}_{1-x}\text{As}$ layers of various compositions was carried out to investigate the strain relief processes in the $\text{In}_x\text{Ga}_{1-x}\text{As}/\text{GaAs}$ material system. These materials were characterized via transmission electron microscopy, X-ray diffraction, electron microprobe, photoluminescence, absorption, and Hall-effect analyses.

A multi-stage strain-relief buffer system was developed to prevent threading dislocations from reaching high indium content ($x > 0.3$) $\text{In}_x\text{Ga}_{1-x}\text{As}$ epitaxial layers. Cross-sectional and planar transmission electron microscopy studies revealed high indium content $\text{In}_x\text{Ga}_{1-x}\text{As}$ epitaxial layers grown on such a buffer system to have a dramatic reduction in dislocation density, with best values being in the 10^6 cm^{-2} range, in sharp contrast to layers grown directly on GaAs substrates. These $\text{In}_x\text{Ga}_{1-x}\text{As}$ epilayers also exhibited excellent electronic properties. For example, Hall-effect measurements on buffered $\text{In}_{0.4}\text{Ga}_{0.6}\text{As}$ layers indicated the room-temperature electron concentrations to be around $5 \times 10^{15} \text{ cm}^{-3}$ while electron mobilities were around $4,500 \text{ cm}^2 \text{ V}^{-1} \text{ s}^{-1}$. Strong band-edge photoluminescence was recorded from such buffered epilayers, the luminescence peak occurring at $1.4 \mu\text{m}$ at room temperature and having a linewidth around 7 meV at 13K.

The efficacy of the designed buffer system is evidenced by the fabrication for the first time of a high sensitivity, planar $\text{In}_{0.4}\text{Ga}_{0.6}\text{As}/\text{GaAs}$ p-i-n photodetector presenting a quantum efficiency of 42%, a responsivity of 0.45 A/W at $1.3 \mu\text{m}$, and dark current of $3 \times 10^{-7} \text{ A}$ at -2.5 V , for an active area of $2 \times 10^{-4} \text{ cm}^2$. This result demonstrates the feasibility of the novel growth technique developed in this work for the monolithic integration of optoelectronic devices operating in the $1.0 - 1.7 \mu\text{m}$ wavelength regime with GaAs electronic devices such as MESFETs, for example.

CHAPTER 1 INTRODUCTION

Motivation and Objectives

Semiconductor heterostructures with layers thicker than a few 100 Å require close lattice matching between the epitaxial layers and the substrate to obtain high quality material. The mismatch-related structural defects usually undermine electronic and photonic performance. Thus, a great interest has developed in terms of devising methods to prevent such defects from forming as well as to prohibit them from reaching the active regions of devices.

The $\text{In}_x\text{Ga}_{1-x}\text{As}/\text{GaAs}$ heterostructure system is of interest for application in two important areas. First, this system encompasses a wide range of direct band gaps (0.36 eV for $x = 1$ to 1.43 eV for $x = 0$) and is therefore of interest for optoelectronic applications in the near IR regime. A second area arises from the fact that its high electron mobilities (up to $11,500 \text{ cm}^2 \text{ V}^{-1} \text{ s}^{-1}$ at room temperature in $\text{In}_{0.53}\text{Ga}_{0.47}\text{As}$ grown on InP) [1] lead to the possibility of tailoring electronic and transport properties for high speed device applications [2].

The quaternary compound semiconductor InGaAsP and, also, the ternary compound InGaAs have been extensively

studied as active layer materials for both sources and detectors operating in the 1.0 - 1.7 μm wavelength range. More precisely, lattice-matched systems such as $\text{In}_{0.53}\text{Ga}_{0.47}\text{As}/\text{InP}$ [3] and $\text{In}_{0.74}\text{Ga}_{0.26}\text{As}_{0.58}\text{P}_{0.42}/\text{InP}$ [4-6] have been employed to fabricate lasers and detectors for application in optical fiber communication systems. The most serious difficulty in terms of growing the lattice-matched quaternary system is to control the ratio of As to P such that a uniform composition is obtained [7]. In addition, despite the fact that InP provides a perfect lattice match to these alloy materials, defect densities in InP wafers are considerably higher than in GaAs, and also InP wafers are considerably more expensive than GaAs wafers. Moreover, integration of discrete InP based devices with presently highly developed GaAs integrated circuits (ICs) is a difficult problem.

Therefore, lasers and detectors operating in the 1.0 - 1.7 μm wavelength range which could be monolithically integrated with GaAs ICs would be highly desirable. The major difficulty with such an approach is that large lattice mismatches exist between GaAs and the particular active layer materials of interest.

The primary objective of this investigation was to develop a technique which could be employed to grow device-quality, high indium content $\text{In}_x\text{Ga}_{1-x}\text{As}$ epitaxial layers on GaAs substrates which could make such a monolithic integration approach feasible.

Literature Survey

Introduction

The importance of compound semiconductors in microelectronics and optoelectronics is primarily based on [8]:

- the particularly suitable electrical or optical properties of these materials (band gap, electron mobility, etc.)
- the ability to tailor these properties to those desired by forming ternary or quaternary compound semiconductor alloys and/or
- the ability to form heterojunction structures of two or more different compounds.

In the least complex applications, nothing more than high-quality bulk substrate material may be required. For more complex device structures, such as heterojunction high-speed devices (e.g. MODFETs) or light-emitting devices (e.g. multi-quantum well lasers), it is necessary to use sophisticated epitaxial growth techniques such as molecular beam epitaxy (MBE) to produce complex, well-controlled, highly uniform heterojunction material structures.

The compound semiconductors usually consist of the group III elements gallium, aluminum, and indium and the group V elements arsenic, phosphorus, and antimony. It is possible

to obtain a large variation of the band gap using those elements in adequate proportions [9]. For instance, materials such $\text{In}_x\text{Ga}_{1-x}\text{As}$ or related materials present suitable band gaps for near IR optoelectronic applications.

Besides the properties related to the band gap, the compound semiconductors must have adequate structural properties which are strongly dependent on the lattice parameter matching between epilayers and substrate or among the different layers.

Thick-layered heterostructures (with layers thicker than a few 1000 Å) require close lattice matching between layers to obtain high quality material. Although most ternary semiconductors have a continuous range of lattice constants, only a few of them are matched to available binary substrates. On the other hand, it is possible to grow thick, high quality multilayers from mismatched materials if the individual layers are kept very thin as in the strained-layer superlattice.

Strained-layer Superlattices

Strained-layer superlattices (SLSs) are made from constituent semiconductors which have dissimilar lattice constants. These structures have layer thicknesses small enough to ensure that the lattice mismatch is totally accommodated by uniform layer strains, so that no misfit dislocations are generated at the superlattice interfaces [2].

The primary advantage associated with SLs is that lattice-matched materials are not required, and for layer thicknesses less than some strain-dependent critical value, dislocation-free SLs are possible [10]. An important consequence of this fact is that it is possible to tailor superlattice material properties, which include structural, optical, and transport properties of these materials [11] to suit specific device applications. This allows the realization of an extremely large number of combinations of such properties. A large variety of energy band diagrams is possible. For instance, through the use of band gap grading one can obtain, starting from a basic energy band diagram, practically arbitrary and continuous variation of this diagram. An effective way to achieve band gap grading, in a system such as InAs/GaAs or $\text{In}_x\text{Ga}_{1-x}\text{As}/\text{GaAs}$ is by growing an InAs/GaAs or $\text{In}_x\text{Ga}_{1-x}\text{As}/\text{GaAs}$ superlattice with spatially varying period so that the average composition and band gap vary with position.

Strain Relief Mechanisms

It is generally accepted that the maximum thickness of a pseudomorphic film, in single layer form, is determined by the balance between the generation of misfit dislocations and the elastic strain built up in the film. At a critical layer thickness, the elastic strain is totally or partially relaxed by the generation of misfit dislocations. Not only the layer

thickness and the lattice mismatch, but also the epitaxial growth temperature and the dislocation line tension are important in defining the concept of critical thickness [12]. However, it is not clear whether or not, for a SL, the critical thickness of the total structure remains the same as that of a single heterostructure. Theoretical calculations have shown that in a SLS, the thickness of the individual layers can be several times larger than that in a single heterojunction, before dislocations are generated [13,14].

Petroff [15] proposes that control over the introduction of misfit dislocations can be achieved by

(a) keeping the film thickness below the critical value, h_c .

(b) producing unidirectional arrays of misfit dislocations as an efficient means of eliminating the dislocations from the epitaxial layers [16].

(c) abrupt step grading of the film composition before reaching that desired for the active layer in the structure [17]. This abrupt change in lattice parameter also produces a bending of the dislocations in the plane of the interface and their elimination by glide to the edge of the crystal.

The misfit dislocations can be introduced by glide or climb of substrate dislocations. The equilibrium spacing between these dislocations is given by $D \approx |b|/\epsilon$ where b is the misfit dislocation Burgers vector and ϵ the misfit strain. A critical thickness h_c is needed before the misfit stress is

sufficient to introduce misfit dislocations and can be approximated for epitaxial layers with similar elastic constants as $h_c \approx |b|/2\epsilon$ [15].

Recent results [18] show that for low In concentrations ($x = 0.05$) in mismatched $\text{In}_x\text{Ga}_{1-x}\text{As}/\text{GaAs}$ interfaces, threading dislocations and possibly dislocation multiplication are the only active misfit dislocation nucleation sources. Grown-in dislocations in the substrate can thread through the epilayer during growth. When the critical layer thickness is exceeded, the threading dislocations glide in the epilayer until they reach the wafer edge, leaving a misfit dislocation at the interface. During its travel to the edge, a misfit dislocation which is forming along the interface can cross perpendicular $\langle 110 \rangle$ misfit dislocations. If the dislocations have the same Burgers vector, a repulsive reaction occurs at the intersection in which part of the dislocation intersection can be bent closer to the surface and away from the interface. If the epilayer is thin, this segment can be attracted to the surface due to the surface image force. When the segment reaches the surface, new free-ended dislocations are created. The free-ended dislocations can glide to produce more misfit dislocations. This process is described in detail by Hagen and Strunk [19].

Strained $\text{In}_x\text{Ga}_{1-x}\text{As}/\text{GaAs}$ SLs with and without a lattice-matching intermediate buffer layer have been grown to investigate the generation and propagation of misfit

dislocations. In strained SLs with a buffer layer, a misfit dislocation network is generated at the substrate/buffer layer interface [12]. The strain in the $\text{In}_x\text{Ga}_{1-x}\text{As}/\text{GaAs}$ SL matched to the InGaAs buffer layer depends on both the indium composition and the thickness ratio of the materials comprising the SL. Since each strained layer is thinner than the critical thickness, no new misfit dislocations are generated in the SL material.

On the other hand, very few or no misfit dislocations could be seen by XTEM in samples grown without the intermediate buffer layer. Only a few dislocations were observed close to the interface between the strained SL and the GaAs buffer layer. These dislocation loops formed in regions of high local stress may grow under misfit stress to generate dislocation networks. The directly grown SL is predominantly in a metastable state in which the whole SL remains coherently strained [12].

A study of misfit dislocations in an $\text{In}_{0.15}\text{Ga}_{0.85}\text{As}/\text{GaAs}$ SLS showed that the buffered SL is an efficient barrier to the propagation of dislocations coming from either the substrate (threading dislocations) or the buffer/SL interface, where the misfit dislocation network is confined [20]. The partial plastic relaxation of the structure is accompanied by the generation and multiplication of glissile dislocation half loops in the GaAs buffer layer and substrate. This probably reflects the particular distribution of the stress

field induced by the mismatch across the interface in both the substrate and relaxed multilayer. Planar TEM samples showed an orthogonal array of misfit dislocations parallel to the $[110]$ and $[1\bar{1}0]$ directions. Cross-sectional TEM analysis showed that most misfit dislocations are confined to the buffer layer/superlattice interface, the superlattice itself being essentially dislocation-free.

Fitzgerald et al. [21] found that the critical thickness was consistent with theoretical calculations of Matthews et al. [22], but the dislocation density at the mismatched InGaAs/GaAs interface was much lower than expected from theory. In highly dislocated InGaAs/GaAs interfaces, dislocations seem to propagate away from the interface due to interdislocation forces which develop as the result of a nonideal distribution of Burgers vectors. Because of the elastic strain force on the epilayer side of the interface, the dislocations are preferentially expelled onto the GaAs side of the heterojunction.

The surface lattice parameter of the $\text{In}_x\text{Ga}_{1-x}\text{As}$ epilayers is equal to that of the GaAs substrate until the film thickness exceeds its critical value [23]. Once this happens, the lattice parameter of $\text{In}_x\text{Ga}_{1-x}\text{As}$ increases abruptly and becomes close to the bulk $\text{In}_x\text{Ga}_{1-x}\text{As}$ lattice constant calculated from Vegard's law.

The calculation of the critical thickness (h_c) for the generation of misfit dislocations was performed by Van der

Merwe [24], and People and Bean [25] based on the energy balance theory, while Matthews and Blakeslee [26] calculated it using the mechanical equilibrium theory.

In order to examine which theory is applicable to the case of InGaAs growth on (001) GaAs, Orders and Usher [27] measured X-ray rocking curves of InGaAs epilayers grown on GaAs for various thicknesses and estimated h_c values from the dependence of the lattice parameter on layer thickness. They found that the values agreed with the theory of People and Bean. Fritz et al. [28] performed photoluminescence spectroscopy and Hall effect measurements on GaAs/In_{0.2}Ga_{0.8}As/GaAs single quantum well structures, estimating the h_c value from the dependence of PL intensity and its half width and electron mobility on the quantum well thickness. The h_c values were found to agree with a calculation made using the Matthews and Blakeslee model.

Nakao and Yao [23] reported a RHEED investigation of the surface lattice parameter and growth mechanism of In_xGa_{1-x}As epilayers grown on (001) GaAs. They used high substrate temperatures (480°C) and found that h_c for various x values ($0.23 \leq x \leq 1$) were placed between the calculations based on the models of Matthews and Blakeslee [26] and Van der Merwe [24]. The 2D-growth mode was confirmed to be dominant at the initial stage of heteroepitaxy, and 3D-growth was triggered by misfit dislocations. Figure 1 presents calculated h_c values using the People and Bean, Matthews and Blakeslee and van der

Merwe models (solid lines) and some experimental results (after Nakao and Yao [23]).

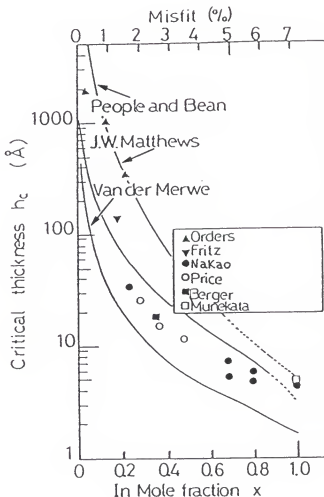


Figure 1.1 Critical thickness (h_c) versus In content (x) for $\text{In}_x\text{Ga}_{1-x}\text{As}$. The points represent some experimental results (figure from Nakao and Yao [23]).

Strain-induced Modifications of Semiconductor Properties

It is possible to grow high-quality epitaxial heterostructures between materials which differ in lattice constant by several percent. This lattice mismatch can be accommodated by uniform lattice strain in sufficiently thin layers. Such a pseudomorphic structure is characterized by an in-plane lattice parameter which remains the same throughout the structure. The strains can cause profound changes in the material properties and therefore provide extra flexibility in device design. Knowledge of the discontinuities in valence and conduction bands at semiconductor interfaces is essential for the analysis of the properties of any heterojunction but has remained rather limited due to experimental difficulties, and the absence of reliable theoretical predictions.

In order to correctly determine the electronic band structure of SLSs it is, in general, necessary to include the appreciable shifts and splitting of the bulk energy bands due to the layer strains [29]. For (001) oriented SLSs, the layer strains can be resolved into hydrostatic and (001) uniaxial components [30]. These strains affect the InGaAs SLS band gaps by shifting the bulk conduction-band minima of the layers (which form the quantum wells associated with the SLS conduction-band minimum) and by splitting the bulk valence-band maxima (which forms two sets of quantum wells associated with the SLS valence-band maxima) [31].

Chang et al. [12] performed low-temperature photoluminescence (PL) and absorption measurements in $\text{In}_x\text{Ga}_{1-x}\text{As}/\text{GaAs}$ MQW grown by MBE to ascertain the optical quality and built-in strain in the heterostructures. Their result showed that biaxial compressive strain in the InGaAs wells increased both the fundamental band gap E_g , and the separation, δE_o , between the heavy- and light-hole excitonic resonances. In MQW grown directly on GaAs, both these energy values were higher than in the samples grown on a intermediate composition buffer layer.

Utilization of Modified Properties Created by Strain

Three important characteristics of SLSs set them apart from the more commonly studied lattice-matched superlattices:

(a) they can be made from a wide variety of constituent materials, allowing their properties to be tailored to specific applications;

(b) their built-in strains can significantly alter their electronic band structures and affect device operation;

(c) they can act as dislocation filters, blocking the propagation of threading dislocations from the substrate into the active region of a device.

Regarding this last characteristic, it has been shown that dislocation-free SLSs can be grown on a mismatched substrate provided their layer thicknesses are smaller than the critical value. This critical value may be very small (a

few Å) when the mismatch is large. In order to grow SLSs with thicker layers, Orders and Usher [27] suggest that a buffer layer can be grown, interposed between the GaAs substrate and the SLS, with a lattice constant graded from that of the substrate to the natural (unsupported) lattice constant of the SLS. This buffer layer is highly dislocated. The main body of the SLS is free of dislocations because the first few SLS periods act as a dislocation filter. The filtering action comes from the alternating strain field of the SLS, which forces threading dislocations to bend over and propagate laterally to the edges of the sample. Dislocation-free SLSs can also be grown using single-composition or step-graded buffers [32,33].

In_xGa_{1-x}As Growth by MBE

MBE is an ultra-high vacuum technique which basically involves the reaction of one or more thermal beams of atoms or molecules with a crystalline surface held at an adequate temperature. This technique allows close control of the growth parameters by precise computer-controlled operation of shutters in front of the effusion cells. Layer compositions are determined by controlling the beam flux ratios of the desired species and the substrate temperature. A key feature of this process is a characteristic smoothing of the growing layer surface. Thus, after a certain period of growth, films which are microscopically smoother than the starting substrate

can be achieved, as evidenced by RHEED observations. Growth rates are usually low (typically about 2 to 6 Å s⁻¹) which reduces the temperature required to achieve epitaxial growth [34] and permits very precise control of layer thicknesses in the range of monolayers (a few Å).

This process can satisfy the most important requirements for the production of high-speed III-V compound semiconductor devices: abrupt planar interfaces, precise composition and well controlled doping profiles [9,35]. The reduced growth temperatures minimize the disturbance of the built-in composition profiles because of bulk diffusion.

The most important considerations for the growth of high-quality crystals are (i) source material purity; (ii) growth parameters; and (iii) lattice-matching to the substrate [36]. Assuming that the purest available source materials are used, we will consider here the growth parameters and lattice-matching influences.

Epitaxial growth involves a series of events [9]:

- (1) adsorption of the constituent atoms and molecules;
- (2) surface migration and dissociation of the adsorbed molecules;
- (3) incorporation of the atoms to the substrate resulting in nucleation and growth.

The last event above is related to the sticking coefficient of each element at the substrate temperature. Arsenic has a very low sticking coefficient above 500°C unless

it is combined with another metal element, say gallium, to form a compound. In the case of GaAs, stoichiometry is attained as long as an excess of arsenic is supplied at the growing surface. The arsenic atoms which do not form a bond to gallium atoms will simply reevaporate from the surface. However, in the case of growing ternary compounds such as $\text{In}_x\text{Ga}_{1-x}\text{As}$ precise ratios of the beam fluxes are required to grow the compound with desired compositions [9].

Growth temperature considerations

It is very difficult to measure accurately the true growth temperature in MBE systems. Using spring loaded contact thermocouples can produce variable results due to varying degrees of contact, whereas the use of an infrared pyrometer depends on the transmission of the view-ports and on the emissivity of the substrate. Thus, the temperature should be considered as relative rather than absolute.

A thorough study to obtain a general unified guideline for the optimum growth temperature of various III-V compounds has been carried out based on the Vegard rule for connecting the congruent sublimation temperatures (T_{cs}) of the bounding binary compounds [37]. From Hall-effect, deep-level transient capacitance, and PL spectroscopy measurements, it is clear that most III-V binary layers grown significantly below their respective T_{cs} are severely degraded, and high-quality films are obtained at growth temperatures above their T_{cs} . Thus, congruent sublimation temperatures serve as a starting point

in choosing the growth temperature of the desired III-V compound [1].

In the $\text{In}_x\text{Ga}_{1-x}\text{As}$ ternary compound one can analyze the effect of substrate temperature on the constituent InAs growth rate (or, equivalently, the indium incorporation rate). It is seen that the InAs growth rate at a fixed indium source temperature remains fairly constant for temperatures below 560°C but drops almost linearly with increasing temperatures above 560°C with a dropping rate of $\approx 1\%$ per 1°C . For growth temperatures relatively high ($> 580^\circ\text{C}$) Auger electron spectroscopy measurements indicate that the indium atoms not incorporated in the InAs compound reside on the surface of the as-grown layer [38].

As/(M) flux ratio

The $\text{As}/(\text{M}=\text{Ga}+\text{In})$ flux ratio during MBE growth has been shown to have significant effects on $\text{In}_x\text{Ga}_{1-x}\text{As}$ material quality. For a fixed temperature, the PL intensity is generally higher for lower ratios, although it is universally accepted that an As-stabilized condition should be maintained [9]. The $\text{As}/(\text{M})$ flux ratio also influences the loss of indium from the growing surface. Indium loss can be suppressed by high arsenic flux; however, high arsenic cell temperatures lead to high background doping levels [39].

Growth of strained $\text{In}_x\text{Ga}_{1-x}\text{As}$ material

The effect of strain on the growth mode is worthy of consideration. Surface lattice relaxation and growth modes of

$\text{In}_x\text{Ga}_{1-x}\text{As}$ on GaAs have been analyzed using the RHEED technique [40]. The surface lattice constant of the $\text{In}_x\text{Ga}_{1-x}\text{As}$ epilayers is equal to that of the GaAs substrate until the film thickness exceeds its critical value. In this case, the lattice parameter increases abruptly and becomes close to the bulk $\text{In}_x\text{Ga}_{1-x}\text{As}$ lattice constant. This is obviously due to the relaxation of misfit lattice strain as a result of the generation of dislocations [23]. Simultaneously with that relaxation, three-dimensional growth takes place and after the strain is almost fully relaxed, the growth mode gradually changes from three- to two-dimensional due to a coalescence of the islands [41,42]. It is clear that strain plays a key role in controlling the growth mode. Thus, the optimum growth conditions for lattice-matched and strained-layer systems can be quite different.

Scope of Present Work

The present dissertation is organized into six chapters. In Chapter 1, a statement of the problem studied is presented. A survey of the most pertinent publications related to this work is also presented.

Chapter 2 describes the methodology, as well as the environment, apparatus, and general experimental procedures adopted during growth of all structures studied.

In chapter 3, the substrate preparation procedures and growth and characterization of GaAs and AlGaAs epitaxial layers are discussed.

Chapter 4 describes the growth and characterization of thick $\text{In}_x\text{Ga}_{1-x}\text{As}/\text{GaAs}$ layers having a wide range of compositions. In this chapter the concept of "critical composition" is introduced and a brief explanation regarding its potential application to the design of multi-stage buffer structures is presented.

In chapter 5, a novel approach to growing device-quality $\text{In}_{0.4}\text{Ga}_{0.6}\text{As}$ epitaxial layers on GaAs involving the controlled propagation of dislocations via a multi-stage strain-relief buffer system is presented and discussed. The various steps taken during the development of this complex buffer system as well as the extensive characterization carried out are also discussed.

Chapter 6 summarizes the principal conclusions of this investigation, including recommendations for further study in this area.

CHAPTER 2
MOLECULAR BEAM EPITAXY: SYSTEM CONFIGURATION
AND CALIBRATION

Introduction

The molecular beam epitaxy (MBE) crystal growth technique is a sophisticated form of evaporation under ultrahigh-vacuum conditions in which precisely controlled quantities of constituent elements and dopants are directed in the form of molecular beams towards a suitably heated single-crystal substrate where epitaxial growth takes place. Since growth rates are usually low (2 to 5 Å/s), and, since the molecular beams can be individually shuttered, highly complex multi-layered structures can be engineered by this technique, such as superlattices, for example, with control provided on the atomic level. Furthermore, since dopant elements are co-evaporated with the constituent elements, precise tailoring of dopant profiles is possible by suitably controlling dopant effusion cell temperatures.

Inside the system growth chamber, constituent and dopant elements are contained in crucibles placed in high temperature furnaces. The furnaces indirectly heat the material to the point of evaporation, producing thermal energy molecular (or atomic) beams which then deposit onto the

substrate. Continuous changes in chemical composition are achieved by programmed variation of furnace temperatures. Abrupt changes are obtained using shutters placed between furnaces and the substrate.

This chapter describes the method, environment, apparatus, and general experimental procedures adopted during growth of all studied structures.

Varian GEN II MBE System Configuration

All of the structures referred to in this work were grown in a Varian Modular Gen II MBE system. This system is comprised basically of three connected vacuum chambers, named growth chamber, buffer chamber, and entry/exit chamber, to which a variety of vacuum, epitaxy and analysis equipment is mounted. Electronic controls for the vacuum, epitaxy and analysis are consolidated into two separate locations: within the system main-frame, and in an electronics cabinet.

Different types of pumps are used to maintain the low pressures required for the processes carried out in each chamber. Some pumps are used for achieving low-vacuum pressure, defined as a pressure in the range between atmospheric pressure and approximately 10 milli Torr. The other pumps are used for attaining high-vacuum and ultrahigh-vacuum pressures (1×10^{-8} to 1×10^{-10} Torr).

Two molecular-sieve roughing pumps evacuate the growth chamber, the entry/exit chamber, and the buffer chamber at any

one time. The pressure in the roughing manifold is measured by a thermocouple (TC) gauge.

The three vacuum chambers (growth, buffer and entry/exit chambers) are pumped to lower pressures by dedicated high-vacuum pumps. The growth chamber uses three pumps to reach high-vacuum, and ultimately, ultrahigh-vacuum. These pumps, mounted on the vacuum sump, comprise a 400 l/s VacIon pump, a titanium sublimation pump, and a cryogenic pump. In the buffer chamber two pumps operate: a 200 l/s VacIon pump, and a titanium sublimation pump. The entry/exit chamber is pumped down to high-vacuum with a small CTI 100 cryogenic pump. The pressure is measured independently by ion gauges placed in each chamber.

The entry/exit chamber allows the loading and unloading of substrates into and out of the system while maintaining the buffer and growth chamber under ultrahigh vacuum conditions. Substrates are loaded onto a transfer mechanism ("trolley") in the entry/exit chamber. This mechanism is transferred into and out of the buffer chamber. The entry/exit chamber has two quartz halogen lamps for substrate heating and degassing of atmospheric gases and water vapor.

A separately pumped buffer chamber isolates the growth chamber from the entry/exit chamber environment. It stores substrates on the trolley and allows substrate preparation prior to growth. A heater station allows for substrate

treatment under high-vacuum conditions immediately before epitaxial growth. This treatment includes removing water molecules, part of the surface oxides, etc., which are still present on the substrate surface due to atmospheric contamination. Preparation of one wafer can be carried out while growth on another wafer is occurring in the growth chamber. This is possible because the buffer chamber is isolated from the growth chamber by a gate valve. A magnetically coupled transfer mechanism allows the transfer of wafers to and from the buffer chamber, and into and out of the growth chamber.

The growth chamber houses the substrate during epitaxy. Through its vacuum sump, the growth chamber is connected to the vacuum pumps. The growth chamber configuration includes the following features: a reflection high energy electron diffraction (RHEED) gun, a quadrupole mass spectrometer, a beam flux monitor (nude ion gauge), a continuous azimuthal rotation (CAR) substrate holder, and a substrate and source flange cryoshroud. The RHEED system and the spectrometer are shuttered to minimize their exposure to beam material during growth. The beam flux monitor is mounted at the opposite side of the substrate holder in such a way that it can be placed at the same substrate position during the flux measurements and is rotated 180° away from the direct beam during growth.

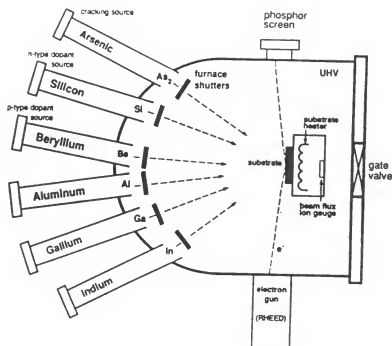


Figure 2.1 Schematic diagram of the Varian GEN II MBE growth chamber configuration

Each source material is placed into a clean crucible made of pyrolytic boron nitride (PBN). The crucible is placed into a tantalum furnace and this furnace is mounted in one of the eight furnace ports on the source flange as indicated schematically in Figure 2.1. Four of the ports are upward-looking. The furnaces placed on these ports have their open ends pointing upward and are used to contain the metals gallium, aluminum, and indium which are kept molten during epitaxial growth. The remaining four ports are down-looking.

A furnace placed in this position contains elements which sublime during growth, such as arsenic, silicon, and beryllium. The furnaces are mounted so that all molecular beams converge at the epitaxial growth position inside the growth chamber. Each crucible has a tungsten-6 wt% rhenium/tungsten-26 wt% rhenium (W-Re) thermocouple attached to its bottom which is kept in permanent contact by spring action. Because each furnace is thermally isolated, its temperature can be controlled precisely and independently. Each furnace has a solenoid-actuated pneumatically driven furnace shutter. Cylindrical ("top hat") crucibles with a capacity of 40 cm³ are used for the metals gallium, aluminum, and indium. Silicon and beryllium, used as dopants, are contained in cone-shaped ("trumpet") crucibles with a capacity of 16 cm³. Arsenic lumps are contained in 60 cm³ cone-shaped crucibles.

A cracking effusion cell model VA-175 designed by EPI Systems was installed in the MBE system to be used with arsenic cylinders. This cell comprises a 160 cm³ capacity pyrolytic boron nitride crucible where the arsenic cylinders are placed and a cracking or dissociation chamber. The bulk evaporator is water-cooled to provide thermal isolation from the cracking zone. The cracking chamber contains a directly heated tantalum filament which accelerates the cracking reaction $\text{As}_4(\text{g}) \rightarrow \text{As}_2(\text{g})$. The crucible and cracking chamber

temperatures are independently controlled by two W-Re thermocouples.

The growth chamber contains a substrate holder mechanism, which includes the continuous azimuthal rotation (CAR) assembly. The substrate mounting block is attached to the CAR assembly on the substrate holder mechanism. With the CAR, the substrate can be manipulated in vacuum from the transfer position to the growth position and vice-versa, and aligned appropriately for performing RHEED analysis. The substrate holder contains heater filaments, which heat the substrate mounting block by radiation through the block back face. A W-Re thermocouple is mounted in a radiation cavity and is shielded from the heater filament. The thermocouple does not physically contact the substrate. The radiation shields minimize direct filament heating of the thermocouple. This thermocouple serves to monitor and aid substrate temperature control precisely during epitaxial growth.

The reflection high energy electron diffraction (RHEED) system is used to monitor oxide desorption prior to growth as well as to determine relative surface concentrations of group III (e.g., gallium) and group V (e.g., arsenic) elements during growth. This equipment is crucial because it is extremely important to know whether the surface is gallium rich or arsenic rich and to monitor surface crystallinity and morphology during epitaxial growth.

The quadrupole mass analyzer is used as a residual gas analyzer to measure background partial pressures and for leak checking the system with helium. This device also provides a means to identify vapor species and their relative abundances.

The beam flux monitor (BFM) is used at the epitaxy position to measure the flux from any effusion furnace. The BFM is mounted 180° from the substrate mounting position on the substrate holder, and consequently, the substrate is not exposed to the molecular beams during flux measurements.

The cryoshroud provides pumping of gas species and dissipation of excess heat within the growth environment.

The MBE Modular Gen II system has some elements controlled by a computer. The computer hardware consists of the following components:

- DEC MICRO/PDP-11/73 process controller with 512 K-Byte random access memory (RAM);
- dual, DSDD 5 $\frac{1}{4}$ " floppy disk drives and a 10 M-byte hard disk drive;
- control console with interface to the MBE system;
- full screen CRT terminal, multifunction keyboard, and dot matrix printer.

The automation system uses the RSX-11M+ (DEC) operating system. The MBE Automation Software version 7.0 enables the grower to consistently produce highly uniform epitaxial growth by controlling the following processes:

- the heating, cooling, and shuttering of the 8 molecular beam furnaces;
- the heating, cooling, positioning and rotation of the substrate;
- the substrate heating in the entry/exit and buffer chambers.

Set-up of the MBE System

The MBE system described previously had just been installed at the beginning of this experimental work, thus some set-up procedures were required to permit growth of the desired structures. Extensive calibration procedures were performed since optimum growth parameters can vary from system to system.

Substrate Temperature Calibration

It is not an easy task to determine the exact substrate temperature during epitaxial growth. Parameters such as substrate doping level, thickness, surface morphology, and mounting method, can change considerably the temperature profile along a cross section of a substrate thus making it difficult to compare growth parameters of structures grown under different conditions. Furthermore, the position of the thermocouple responsible for the temperature monitoring which is located away from the substrate surface contributes to this uncertainty.

To overcome this problem, a substrate surface temperature calibration was carried out using three different temperature monitors. The first monitor was the W-Re thermocouple that is located inside a radiation cavity in the substrate holder and would be used during epitaxial growth (thermocouple number 1). The second monitor was a Chromel/Chromel-Alumel thermocouple kept in contact with the substrate surface by spring action (thermocouple number 2). The third monitor was an infrared pyrometer. The use of these three monitors was required to eliminate the measurement errors due to various degrees of contact between the thermocouple number 2 and the substrate surface as well as its deterioration caused by arsenic action. Furthermore, the use of an infrared pyrometer depends upon the transmission of the view-ports as well as the emissivity of the substrate. The method employed in the measurement considered the first readings taken at low temperatures from the thermocouple number 2, attached to the substrate surface, as correct. These readings were used to set the substrate emissivity and the view-port transmission. The pyrometer was calibrated at 250°C. Both its emissivity and transmission of the view-ports were assumed to be constant over the range of temperatures studied. After this first step, it was observed that there was a reproducible relationship between the pyrometer and thermocouple number 1 readings. The values obtained from the thermocouple number 2, attached to the substrate surface

Table 2.1 Correspondence between monitored temperature (T_{mon}) and actual temperature (T_{ss})

T_{mon}	T_{ss}	T_{mon}	T_{ss}	T_{mon}	T_{ss}	T_{mon}	T_{ss}
285	300	475	450	655	560	797	640
305	320	490	460	670	570	820	650
330	340	520	480	690	580	840	660
350	360	550	500	705	590	860	670
380	380	585	520	725	600	875	680
400	400	600	530	740	610	887	690
430	420	620	540	760	620	900	700
460	440	635	550	780	630	915	710

were time dependent due to the thermocouple progressive deterioration under vacuum and presence of As vapors. The results are presented in Table 2.1.

Effusion Source Preparation Procedures

Before the source materials were loaded, an extensive degassing of the furnaces and crucibles was performed under ultrahigh-vacuum conditions for one hour at the following temperatures:

16 and 40 cm³ crucibles: 1600 °C

60 cm³ crucibles: 1200 °C

Arsenic cracker - 160 cm³ crucible: 800 °C

cracking chamber: 1600 °C

Silicon and beryllium, used as dopants, were loaded into their respective crucibles which were placed in upward-looking positions and heated to 1700°C and 1450°C respectively to melt the charges. Once molten, these materials adhered to the crucible internal walls so that the crucibles could subsequently be repositioned as downward-looking furnaces. The metals gallium, aluminum, and indium, which remain in a liquid state during evaporation, were loaded into upward-looking furnaces, as described previously. Initially arsenic in the form of lumps was used, but this limited its use to upward-looking furnaces. Furthermore, lumps present a large surface area which favors the adsorption of gases and limits consequently the epilayer quality. Later on, an arsenic cracker source which provides the reaction $As_4 \rightarrow As_2$, was installed and used for most growths.

After loading the source elements, the system was pumped down to high-vacuum and a complete bake-out at 200 °C was performed for at least 48 hours to induce desorption of gases and water molecules from the chamber walls, crucibles, and source materials. A few hours were necessary to cool down the chambers following the bake-out procedure.

Each time the source materials were loaded or refilled, a further step was performed, comprising of an extensive degassing at temperatures 80°C above the temperatures normally used during growth for the metals, silicon, and beryllium, and 10°C above the temperatures used

during growth for arsenic. Table 2.2 presents the temperatures used for each material as well as the time consumed during each step.

Table 2.2 Temperature of each furnace during degassing of the source materials after a system bake-out.

Step	Time (hr)	Furnace temperatures at end of step (°C)					
		Ga	Al	In	As	Si	Be
Heating	1	1070	1250	890	300	1350	900
Degassing	1	1100	1280	920	325	1400	940
Cooling	1	250	820	200	90	250	200

An outgassing at similar temperatures was carried out for 10 minutes prior to growth in all furnaces to be employed during the growth. All tasks that involved heating of furnaces or substrate in the growth chamber were performed after liquid nitrogen was allowed to flow through the cryoshrouds for at least 30 minutes. This permitted the dissipation of excessive heat and removal of gases released during heating of the crucibles. After degassing of the furnaces, crucibles, and source materials, the furnaces were cooled down to an idle temperature found to be the best compromise to avoid either excessive evaporation of the elements or adsorption of gases

by those elements during intervals between growths. Aluminum was kept at a high idle temperature in order to avoid its solidification which, if repeated unnecessarily, can lead to crucible rupture.

The system bake-out followed by the extensive degassing procedure was performed each time the growth chamber was exposed to atmosphere.

Substrate and Source Materials Specifications

The substrate material used in this work, namely semi-insulating GaAs single crystal wafers purchased from Sumitomo Electric USA Inc., is specified in Table 2.3.

Table 2.3 Specification of the GaAs substrates

Dopant	none
Resistivity	$\geq 10^7$ ohm cm
Etch pit density	$\leq 50,000$ cm ⁻²
Orientation	2° off (001) → (110) $\pm 0.5^\circ$
Size	50 \pm 1 mm
Thickness	450 \pm 25 mm
Surface finishing	both sides polished

Table 2.4 presents the source materials used as well their degree of purity and manufacturer.

Table 2.4 Specification of the source materials used in the MBE system

Element	Purity	Vendor
Gallium	8N	Alcan Electronic Materials
Aluminum	6N	United Mineral and Chemical Corp.
Indium	7N	United Mineral and Chemical Corp.
Arsenic	7N	Furukawa
Silicon	6N	Johnson Matthey, Inc.
Beryllium	5N	Atomergic Chemetals Corp.

Growth System Calibration

Before epitaxial growth is carried out, some theoretical calculations are necessary in order to determine the parameters of importance, such as the beam equivalent pressure of each constituent element suitable for a particular composition and growth rate. This parameter is dependent upon temperature controller calibration, crucible shape and capacity, and beam flux ion gauge sensitivity. Thus, any theoretical calculation serves only as a starting point to predict the desirable flux for each element. Since an ion gauge does not detect true pressure but rather detects atom or

molecule number densities, a conversion from the artificially calibrated "pressure" reading to absolute density is required.

Theory

In order to simplify the calculations, it is assumed that the element vapors are ideal gases within the framework of the kinetic theory of gases. This is not, obviously, the case as atomic and molecular beams are freely evaporating from heated effusion cells.

The beam density is defined as the number of atoms or molecules per cm^3 and its calculation based on the "pressure" measured by the ion gauge is outlined below [43]:

$$P V = \frac{1}{3} n m C^2, \quad (2.1)$$

$$R T = \frac{1}{3} m C^2, \quad (2.2)$$

$$C^2 = \frac{3 R T}{N_A m} = \frac{3 R T}{M}, \quad (2.3)$$

$$\frac{R}{N_A} = k, \quad (2.4)$$

where P = pressure in dyne.cm^{-2} ;

V = volume in cm^3 ;

n = number of atoms or molecules in volume V ;

m = mass of a single atom or molecule in gm ;

C = root mean square speed;

R = 8.31×10^7 ergs.mole⁻¹.K⁻¹;

N_A = 6.02×10^{23} molecules.mole⁻¹ (Avogadro's number);

M = molecular weight of gas in gm.mole⁻¹;

k = 1.38×10^{-16} erg.K⁻¹ (Boltzmann's constant).

From equations (2.1), (2.2), and (2.3) we obtain

$$PV = \frac{1}{3} nm \frac{3RT}{N_A m} = \frac{nRT}{N_A} . \quad (2.5)$$

Thus, it follows from equations (2.4) and (2.5)

$$\begin{aligned} PV &= nkT, \\ \frac{n}{V} &= \frac{P}{kT} = N, \end{aligned} \quad (2.6)$$

where N is the beam density in number of atoms or molecules per cm⁻³. Since the ionization gauge being used for beam density measurements is calibrated for a particular gas, usually nitrogen at room temperature (300 K), a conversion factor is required to read other beams.

If, for instance, for atoms or molecules of an element x , an ion gauge reading of $P(x)$ is obtained, then

$$N(x) = \frac{N'(N_2)}{I(x)} , \quad (2.7)$$

where $I(x)$, the relative ionization cross section, is a factor relating absolute density to relative density between an atom or molecule of an element x and N_2 and $N'(N_2)$ is the N_2 density which would yield an N_2 pressure measurement of

$$P(N_2) = P(x) . \quad (2.8)$$

From equations (2.6), (2.7) and (2.8) we obtain

$$N(x) = \frac{1}{(300K) k} \frac{P(x)}{I(x)} , \quad (2.9)$$

where $N(x)$ = absolute density of atoms or molecules of element x in cm^{-3} ;

$P(x)$ = "pressure" measured with the ion gauge calibrated for N_2 at 300 K.

The beam flux of an ideal gas is given by the expression

$$J = \frac{Nc}{4} = \frac{NC}{\sqrt{6}\pi} , \quad (2.10)$$

where J = flux in atoms or molecules. $\text{cm}^{-2}.\text{sec}^{-1}$;

c = average speed in $\text{cm}.\text{sec}^{-1}$;

C = root mean square speed in $\text{cm}.\text{sec}^{-1}$ [43].

However, the atoms or molecules are freely evaporating from an effusion cell and cannot be considered in random motion. Thus, if it is assumed that all atoms or molecules in a molecular beam of density N are moving in the same direction with an average speed c and are impinging on a substrate whose normal is tilted an angle θ from the axis of the effusion cell [44], the molecular beam flux in atoms or molecules $\text{cm}^{-2}.\text{sec}^{-1}$ is given by

$$J_{MB} = N c \cos \theta . \quad (2.11)$$

The average speed [43] can be written as

$$C = C \sqrt{\frac{8}{3\pi}} . \quad (2.12)$$

Combining equations (2.3), (2.9), (2.11), and (2.12) one obtains

$$J_{MB}(x) = \sqrt{\frac{8R}{\pi}} \cdot \frac{1}{(300K)k} \cdot \frac{P(x)}{I(x)} \cdot \sqrt{\frac{T(x)}{M(x)}} \cdot \cos\theta . \quad (2.13)$$

If the equation above is written using $\theta = 33^\circ$ and the ion gauge reading $P(x)$ in Torr,

$$J_{MB}(x) = 3.92 \times 10^{20} \frac{P(x)}{I(x)} \sqrt{\frac{T(x)}{M(x)}} [cm^{-2} sec^{-1}] , \quad (2.14)$$

where $T(x)$ = effusion cell temperature in K;

$M(x)$ = molecular weight of the source material in gm mole⁻¹;

$I(x)$ = relative ionization cross section of element x.

The ionization cross section [44] relative to N_2 can be approximated as

$$I(x) = 0.6 \frac{\sum Z}{14} + 0.4 , \quad (2.15)$$

where Z is the atomic number and the summation is over all atoms in x.

GaAs and its related compounds InGaAs and AlGaAs have the zincblende structure. Considering the GaAs example, there

are two layers of GaAs per lattice constant in the (001) growth direction. Therefore, two layers per 5.653 Å (lattice constant a) are equivalent to 3538 layers per μm . If 1 layer of GaAs is deposited per second a growth rate of $1.02 \mu\text{m hr}^{-1}$ is obtained. Since there are two Ga atoms per a^2 in a single layer there are 6.26×10^{14} Ga atoms per cm^2 . Thus, a Ga flux of 6.15×10^{14} Ga atoms per cm^2 per sec is necessary to provide a growth rate of $1 \mu\text{m hr}^{-1}$.

The growth rate theoretically calculated may be obtained by the following expression, using the Ga flux value given by equation (2.14),

$$GR(\text{GaAs}) = \frac{J_{\text{MB}}(\text{Ga})}{6.15 \times 10^{14}} \quad [\mu\text{m hr}^{-1}]. \quad (2.16)$$

It is worthwhile to stress here that, due to the many assumptions made in the calculation above, the values theoretically obtained serve as a starting point to determine the appropriate pressure readings which will at last be used to obtain a particular composition and growth rate.

An efficient way to experimentally determine the absolute flux of a molecular beam at the substrate position is to choose a suitable beam equivalent pressure for an element and grow a layer of this element for a definite amount of time. Thickness measurements will provide the growth rate for that element at the flux of choice. By knowing its crystal structure it is possible to determine the absolute flux.

An alternative method which works well for the compounds of interest is to choose a certain flux for each metal and grow the binary compounds GaAs, AlAs, and InAs. In this case one needs to assume the arsenic incorporation rate is just the one necessary to grow stoichiometric or near-stoichiometric compounds (50% metal - 50% arsenic). To obtain stoichiometry, arsenic must be supplied in excess. This excess will prevent any arsenic depletion at the growth temperature. The growth rate of the compound is related to the beam flux of each metal. By comparing the crystal structures of each binary compound it is possible to estimate the metal beam flux ratio necessary to grow a ternary or quaternary epilayer with a particular composition.

In order to avoid excessive delays before growth, waste of source materials or even prevent unnecessary pauses during growth of complex structures a correlation between source temperatures and beam equivalent pressures is very desirable. Some points should be taken into consideration when establishing this correlation: (i) the temperature controllers should be able to maintain a very stable temperature providing a constant molecular beam flux during growth; (ii) the flux reading may change after either a new source material charge is loaded or the ionization gauge is replaced; and (iii) the beam equivalent pressures may change significantly each time the temperature controllers are recalibrated. Therefore, such a correlation should never be considered as absolute and

frequent checks are necessary to ascertain the proper growth rate parameters.

Flux Calibration

The gallium, aluminum, and indium beam equivalent pressures as a function of crucible temperatures were established experimentally for this system. For each metal, a temperature range was used to obtain the corresponding pressures. Before beginning the flux measurements, each furnace was outgassed at a temperature at least 50°C above the highest temperature to be used during the measurements, for 20 minutes. A background pressure lower than 2×10^{-9} Torr was observed during the experiment. The furnaces were set to the intended temperatures and allowed to equilibrate for about 20 minutes before any reading was taken. The beam flux ion gauge was placed at the growth position and the readings were taken five times for each furnace with the individual shutters opened and closed. The beam equivalent pressure was the difference between the two readings ($P_{\text{open}} - P_{\text{closed}}$). The results are presented in Table 2.5, Table 2.6, and Table 2.7.

If the beam equivalent pressure (BEP) is plotted in a logarithmic scale against the inverse of absolute temperature a straight line is obtained (see Figure 2.2).

Table 2.5 Gallium Beam Equivalent Pressure (BEP) as a function of furnace temperature

T (°C)	$10^3/T(K)$	BEP (10^{-7} Torr)	log BEP
1000	0.7855	1.93	-6.71
1010	0.7794	2.28	-6.64
1020	0.7734	2.68	-6.57
1030	0.7675	3.13	-6.50
1035	0.7645	3.30	-6.48
1040	0.7516	3.68	-6.43
1050	0.7559	4.19	-6.38
1060	0.7502	4.88	-6.31
1070	0.7446	5.60	-6.25
1080	0.7391	6.44	-6.19
1090	0.7337	7.28	-6.14
1100	0.7283	8.38	-6.10

These two parameters obey a relationship of the form

$$BEP = A \exp\left(-\frac{B}{kT}\right), \quad (2.17)$$

where A and B are constants. Writing this expression in a more suitable way, the following equations were obtained for Ga, Al, and In furnace temperatures as a function of the desired

beam equivalent pressure:

$$T_{Ga} (^{\circ}C) = \frac{11101}{2.01 - \log BEP (Ga)} - 273, \quad (2.18)$$

$$T_{Al} (^{\circ}C) = \frac{15280}{3.703 - \log BEP (Al)} - 273, \quad (2.19)$$

$$T_{In} (^{\circ}C) = \frac{9727}{2.03 - \log BEP (In)} - 273. \quad (2.20)$$

In a similar manner, the arsenic flux dependence upon As furnace temperature was determined. In this case, the cracking filament must be heated up to 900°C before the As crucible is heated. For the first operation of the As cracker, the residual gas analyzer was turned on after stabilization of the As crucible temperature. For cracking filament temperature of 900°C, the As_1/As_2 peak ratio was 1.29 indicating a very good cracking efficiency. No As_4 peak was detectable.

For the arsenic cracker, the furnace temperature as a function of the desired beam equivalent pressure is given by

$$T_{As} (^{\circ}C) = \frac{7686}{8.10 - \log BEP (As)} - 273. \quad (2.21)$$

Table 2.8 presents the data obtained for the arsenic cracker. As BEP is plotted versus As cracker temperature in Figure 2.3.

Table 2.6 Aluminum Beam Equivalent Pressure as a function of Al furnace temperature

T (°C)	$10^3/T(K)$	BEP (10^{-7} Torr)	log BEP
1110	0.7231	0.46	-7.34
1120	0.7179	0.55	-7.26
1130	0.7128	0.66	-7.18
1140	0.7077	0.77	-7.12
1150	0.7027	0.89	-7.05
1160	0.6978	1.11	-6.96
1170	0.6930	1.27	-6.90
1180	0.6882	1.56	-6.81
1190	0.6835	1.76	-6.75
1200	0.6789	2.16	-6.67
1210	0.6743	2.42	-6.62
1220	0.6698	3.12	-6.51

Table 2.7 Indium Beam Equivalent Pressure as a function of In furnace temperature

T (°C)	$10^3/T(K)$	BEP (10^{-7} Torr)	log BEP
800	0.9320	0.89	-7.05
810	0.9234	1.08	-6.97
820	0.9149	1.34	-6.87
830	0.9066	1.61	-6.79
840	0.8985	1.95	-6.71
850	0.8905	2.37	-6.63
860	0.8826	2.84	-6.55
870	0.8749	3.37	-6.47
880	0.8673	4.10	-6.39
890	0.8598	4.62	-6.34
900	0.8523	5.37	-6.27
910	0.8453	6.30	-6.20

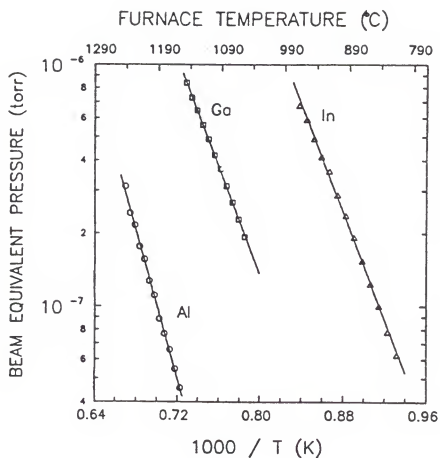


Figure 2.2 Beam Equivalent Pressure of metals versus furnace temperature

Table 2.8 Arsenic Beam Equivalent Pressure as a function of As furnace temperature

T (°C)	$10^3/T(K)$	BEP (10^{-7} Torr)	log BEP
312.0	1.721	0.92	-5.04
313.5	1.705	0.99	-5.01
315.0	1.701	1.05	-4.98
317.0	1.695	1.21	-4.92
317.4	1.694	1.24	-4.91
318.0	1.692	1.25	-4.90
318.5	1.691	1.29	-4.89
319.0	1.689	1.24	-4.91
319.3	1.688	1.30	-4.89
319.5	1.688	1.34	-4.87
320.7	1.684	1.40	-4.85
321.5	1.682	1.53	-4.82

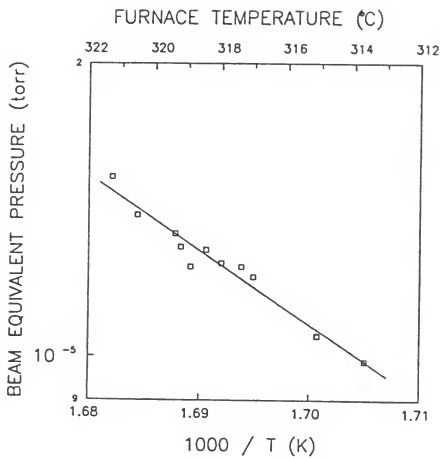


Figure 2.3 Arsenic Beam Equivalent Pressure as a function of As furnace temperature

CHAPTER 3

GROWTH AND ELECTRICAL CHARACTERIZATION OF GaAs AND AlGaAs EPITAXIAL LAYERS

Growth of GaAs and AlGaAs epilayers was performed in order to determine the optimum growth conditions to be employed in the Varian MBE system. Electrical characterization by Hall-effect measurements gave an evaluation of material quality, so that more complex structures, for instance, ternary compounds not lattice-matched to GaAs substrates, could later on be grown under the best known conditions. In this chapter, epilayer growth and substrate preparation procedures are described and the results of the electrical measurements reported.

Substrate Preparation Procedures

This section will describe the substrate preparation procedures used prior to growth and include a brief description of some experiments carried out to determine the best conditions to prepare a substrate for growth.

The first preparation step involved exposure of the GaAs wafer surfaces to an ultraviolet light/ozone environment for 2 minutes. This procedure leads to the formation of a stable carbon-free oxide layer which serves to protect the

underlying GaAs from atmosphere contaminants [45,46]. It was determined that a time longer than two minutes induces the formation of a thicker oxide layer which is more difficult to remove during in-situ substrate heating.

After being exposed to uv/ozone, the wafers were attached to molybdenum blocks with indium. The blocks were loaded into the trolley and blown with dry nitrogen to remove any particles from the substrate surfaces. The trolley was introduced into the entry/exit chamber which was pumped down. When the pressure was lower than 1×10^{-7} Torr the chamber was heated to 200°C for 30 minutes and allowed to cool down until the pressure dropped to 5×10^{-8} Torr. The trolley was then transferred to the buffer chamber where each substrate was individually heated to 450°C for 20 minutes immediately before being transferred to the growth chamber. This occurred after the pressure had dropped to less than 5×10^{-8} Torr. In the growth chamber, the substrate was heated slowly up to 650°C and left at this temperature for 5 minutes under arsenic overpressure. The RHEED system was used to monitor oxide desorption after which the substrate temperature was lowered to the appropriate growth temperature. All substrate temperatures referred in this work are the real temperatures determined by the method described in the previous chapter.

It is useful at this point to discuss the reflection high-energy electron diffraction (RHEED) technique which is a very useful tool to employ before and during growth. The GaAs

wafers used in this experimental work were cut from a cylinder in such a way that the surface where epitaxial growth would take place belonged to the (001) plane. When the electron beam reaches the substrate surface at a very shallow angle it produces a diffracted pattern which is observed on a screen suitably located opposite the electron gun. This pattern varies according to the substrate position in relation to the beam [1]. Figure 3.1 shows the possible directions where the substrate may be placed to determine the substrate cleanliness and growth conditions.

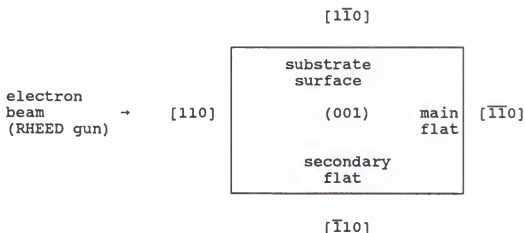


Figure 3.1 Substrate orientation during RHEED pattern observation

The RHEED pattern of a flat oxide-free (001) GaAs surface observed when the electron beam is incident from one

of the four directions indicated in Figure 3.1 comprises of elongated spots which are related to the crystal structure. The spot length is related to surface flatness, the shorter the spots the rougher the surface.

Surface reconstruction appears usually after a few layers are deposited and seldom after oxide desorption and before growth [47]. This surface reconstruction can be detected by extra lines which appear between the elongated spots. Second-order reconstruction presents an extra line and fourth-order presents three extra lines between the usual streaks. An arsenic-rich surface presents either a second-order reconstruction when the electron beam comes in the $[110]$ or $[\bar{1}\bar{1}0]$ direction or a fourth-order reconstruction in the $[1\bar{1}0]$ or $[\bar{1}10]$ direction. An arsenic-deficient surface presents the same types of reconstruction but in the orthogonal azimuth [1,9].

To determine the temperature at which surface oxide desorption occurs, a substrate was heated for 30 min at 450 °C in the buffer chamber and immediately transferred to the growth chamber where it was kept at 550 °C for 60 minutes without arsenic overpressure. The high energy electron diffraction (RHEED) pattern was observed from then on. A pattern comprised of elongated lines ("streaks") was obtained at that temperature. Weak lines were observed between the elongated lines corresponding to a second order reconstruction, characteristic of an arsenic-stabilized

surface [48]. The substrate was then heated slowly up to 650°C and the pattern changes were recorded. At 600°C the weak lines between the strong bulk lines vanished as an indication of a slightly arsenic-deficient surface. Subsequently, at 620°C the bulk line length showed an appreciable decrease indicating progression towards a rough surface. At a higher temperature, 630°C, the pattern was clearly spot-like. At 640°C, the streaks were completely gone. Further temperature increase up to 650 °C did not promote any additional change in the RHEED pattern. It is important to emphasize here that no arsenic overpressure was supplied to the substrate. These changes in the RHEED pattern showed that initially an oxide desorption took place at a relatively low substrate temperature (< 550°C) exposing a flat arsenic-stabilized surface [47]. Substrate heating above 620 °C without arsenic overpressure promoted undesirable arsenic depletion and surface roughening.

Later experiments involving substrate heating for less time (substrates not held at 550°C for an extended period of time as in the case above) and with arsenic continuously supplied to the substrate surface demonstrated that it was possible to reach even higher temperatures (> 650 °C) without surface degradation although a surface reconstruction was barely seen. If the substrate was heated in the buffer chamber at 450°C for 20 minutes and immediately transferred to the growth chamber and heated slowly up to 650°C without being held at a lower temperature it was observed that oxide

desorption occurred at a slightly higher temperature, between 620 and 630°C. Furthermore, if arsenic overpressure was supplied to the substrate surface, no surface roughening occurred.

Growth and Electrical Characterization of GaAs Epilayers

The first growth of GaAs in this system was intended to provide the growth rate as a function of gallium beam equivalent pressure (BEP). The arsenic BEP was chosen to be about 15 times larger than the gallium BEP, in order to avoid any arsenic depletion during epilayer growth. A GaAs epilayer was grown at a substrate temperature (T_{ss}) equal to 600°C, for 1 hr, with BEP (Ga) maintained at 5.1×10^{-7} Torr. A piece of another GaAs wafer was used as a mask to cover part of the substrate so that a step was produced. By measuring the height of this step with a Dektak II-A profilometer the epilayer thickness was determined to be 1.086 μm . Thus, to obtain a growth rate of 1 $\mu\text{m hr}^{-1}$ a BEP (Ga) = 4.7×10^{-7} Torr was necessary. This value depends upon the beam flux ion gauge being used as well its sensitivity. It was later found that the growth rate can be significantly changed when the ion gauge is replaced so that periodic checks are necessary to ascertain the proper growth rate. In a different experiment, a GaAs epilayer was grown with a constant BEP (Ga) but different BEP (As) in order to assess the best flux ratio between the two elements. For the substrate temperature

employed in this growth, $T_{ss} = 600^{\circ}\text{C}$, the RHEED pattern showed the surface reconstruction changed from arsenic- to gallium-stabilized when $\text{BEP(As)}/\text{BEP(Ga)}$ dropped below 5. If a lower BEP (As) was used a roughening of substrate surface would occur. It was observed that surface reconstruction changed from one type to another after growth and with the substrate still kept at growth temperature when the arsenic shutter was closed and opened, indicating that at the usual growth temperatures an arsenic overpressure is necessary during growth intervals to avoid arsenic depletion.

A set of four GaAs samples was grown for 2 hr under the same conditions: $\text{BEP (As)} = 7 \times 10^{-6}$ Torr, $\text{BEP (Ga)} = 4.7 \times 10^{-7}$ Torr except substrate temperatures which were 500, 550, 600, and 650°C , respectively, in order to determine the growth rate dependence on substrate temperature. Thickness measurements showed no significant growth rate variation over the studied temperature range. The RHEED patterns monitored before, during, and after growth, showed (i) the oxide desorption technique presented the same results previously reported; (ii) there was no clear reconstruction before growth, but well defined second- and fourth-order reconstruction lines were observed for $[110]$ and $[1\bar{1}0]$ directions, respectively, after a few minutes of growth, characterizing an arsenic-stabilized surface; and (iii) the RHEED pattern observed during growth at $T_{ss} = 650^{\circ}\text{C}$ presented a surface reconstruction not as good as the corresponding ones obtained at lower temperatures

indicating that arsenic desorption rate was possibly close to its sticking rate at the high substrate temperature.

The next step was to determine the growth conditions necessary to obtain high-quality doped GaAs layers with the desired doping levels.

The dopant beam fluxes obey the same equations previously presented for the other elements but cannot be measured directly since the beam equivalent pressures necessary to provide the desirable doping levels (10^{15} to 10^{19} cm^{-3}) are at least three orders of magnitude lower than the pressures of Ga and As and, consequently, not distinguishable from the growth chamber background pressure. In addition, the presence of contaminants in the growth chamber and impurities in the source materials which are incorporated in the epilayer during growth can cause unintentional doping of undoped epilayers or affect dramatically the compensation ratio in slightly doped layers. Furthermore, there is no guarantee that all atoms coming from the dopant crucible and reaching the substrate will be incorporated in the epilayer for the usual growth conditions.

To overcome this problem, it was assumed that the doping level (n or p) was a function of the form

$$n \text{ (or } p) = A \times \exp(-B/T), \quad (3.1)$$

where T is the absolute temperature of the dopant furnace and

A and B are constants to be determined. A set of samples was grown under the same growth conditions except the dopant source temperature which was changed from sample to sample to cover the range of interest. Table 3.1 and Table 3.2 present the dopant source temperatures used as well the electronic properties determined at room temperature by measuring the resistivity and Hall voltage. The Van der Pauw method was used to perform these measurements. Small pieces of pure indium were placed at the corners of square samples which were heated at 270°C for 5 minutes in a reducing atmosphere (92% N₂ - 8% H₂) to induce a good alloying between indium and substrate.

Table 3.1 Electronic properties of Si-doped GaAs layers.

Si source temperature (°C)	Mobility (cm ² V ⁻¹ s ⁻¹)	Electron concentration (cm ⁻³)	Resistivity (Ω cm)
1080	5944	2.42 E15	4.5 E-1
1099	5822	4.21 E15	2.5 E-1
1128	5770	9.24 E15	1.2 E-1
1174	4820	4.52 E16	2.9 E-2
1204	4611	9.14 E16	1.5 E-2
1258	3230	4.20 E17	4.6 E-3
1287	2945	8.09 E17	2.6 E-3
1353	1900	4.16 E18	7.9 E-4

Table 3.2 Electronic properties of Be-doped GaAs layers.

Be source temperature (°C)	Mobility (cm ² V ⁻¹ s ⁻¹)	Hole concentration (cm ⁻³)	Resistivity (Ω cm)
748	330	5.85 E16	3.2 E-1
771	287	1.22 E17	1.8 E-1
811	204	5.60 E17	5.5 E-2
830	198	8.70 E17	3.6 E-2
895	104	8.22 E18	7.3 E-3
969	81	5.55 E19	1.4 E-3

All doped GaAs epilayers were grown on semi-insulating substrates with a 0.5 μm thick undoped GaAs buffer layer grown first. The substrate temperature and growth rates were respectively 600°C and 1 μm hr⁻¹.

A very good agreement between the experimental data and the exponential function is observed in Figure 3.2. This fact indicates that for the studied doping level range the incorporation rate was proportional to the incident flux and high doping levels can be obtained without saturation. These results agree fairly well with those reported by A. Y. Cho [9] and J. S. Blakemore [49].

The A and B constants of equation (3.1) are obtained from the experimental data. This equation can be written in a more appropriate way for Si- and Be-doped layers:

$$T_{Si} (^{\circ}C) = \frac{26188}{34.7 - \log n} - 273, \quad (3.2)$$

$$T_{Be} (^{\circ}C) = \frac{33689}{17.3 - \log p} - 273. \quad (3.3)$$

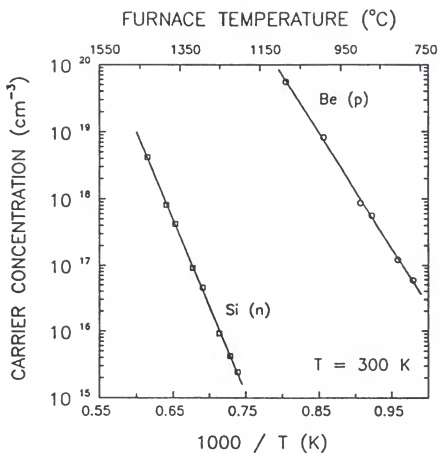


Figure 3.2 Carrier concentration of GaAs layers as a function of dopant furnace temperature.

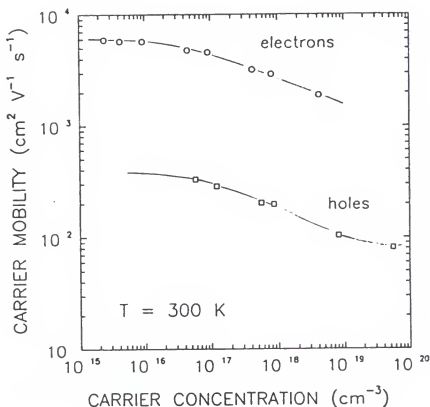


Figure 3.3 Room temperature carrier mobility as a function of carrier concentration in n-type and p-type GaAs layers.

The carrier mobility at room temperature increased as the carrier concentration decreased and presented typical values [1,9] as shown in Figure 3.3.

A different set of Si-doped GaAs layers was grown to determine the optimum growth temperature for GaAs which would provide the best electronic properties. All growth parameters

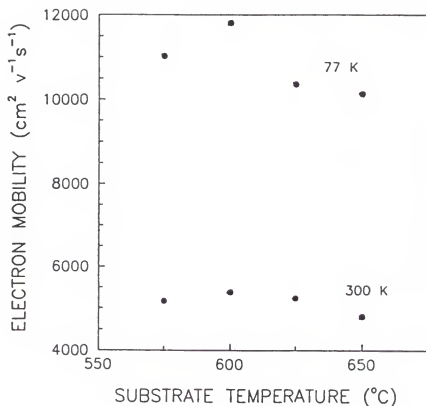


Figure 3.4 Electron mobilities in Si-doped GaAs as a function of substrate temperature (carrier concentration $\approx 2 \times 10^{16} \text{ cm}^{-3}$).

were kept constant except the substrate temperature which varied from 575 to 650°C. Table 3.3 presents the measured properties and Figure 3.4 illustrates graphically the measurements performed at 77 K and 300 K. It is clear that all samples presented reasonable electronic properties although 600°C seemed to be an optimum substrate temperature for GaAs growth.

Table 3.3 Electronic properties of Si-doped GaAs layers as a function of substrate temperature during growth

Substrate temperature (°C)	Mobility ($\text{cm}^2\text{V}^{-1}\text{s}^{-1}$)	Electron concentration (cm^{-3})	Resistivity ($\Omega\text{ cm}$)
575	5169	2.17 E16	5.6 E-2
600	5383	1.77 E16	6.6 E-2
625	5235	1.72 E16	6.7 E-2
650	4798	1.95 E16	6.9 E-2

Growth and Characterization of AlGaAs Epitaxial Layers

AlGaAs layers of various compositions can be grown directly on GaAs substrates by varying the Ga/Al beam flux ratio. To estimate the beam flux ratio necessary to grow an epilayer with a particular composition, the following approach may be used:

(i) consider that an $\text{Al}_x\text{Ga}_{1-x}\text{As}$ epilayer is a mixture of two compounds, namely $(\text{AlAs})_x$ and $(\text{GaAs})_{1-x}$.

(ii) assume, for now, that both compounds have the same lattice parameter, although AlAs has a slightly larger lattice parameter, $a = 5.66 \text{ \AA}$ (0.12% mismatch), as compared to GaAs, $a = 5.653 \text{ \AA}$.

(iii) assume the sticking coefficient of both aluminum and gallium is equal to 1 for the substrate temperature range employed in these growths.

(iv) assume that the arsenic beam flux is sufficient to obtain both stoichiometric compounds (50 at% As) and that arsenic atoms supplied in excess will reevaporate from the growing surface.

Therefore, if an $\text{Al}_x\text{Ga}_{1-x}\text{As}$ layer of unknown x is grown, it is possible to determine x by measuring the layer thickness, using the following expression:

$$x = \frac{GR(\text{AlAs})}{GR(\text{AlAs}) + GR(\text{GaAs})}, \quad (3.4)$$

where $GR(\text{AlAs})$, the growth rate of AlAs, is the difference between the growth rates of the ternary compound and of GaAs.

A heterostructure consisting of multiple layers of GaAs and AlGaAs was grown in order to determine the aluminum beam flux necessary to obtain particular values of x . The growth time was kept constant for all layers so that each growth rate could be easily determined and, consequently, the x value. The gallium beam flux was also maintained constant throughout the growth and each AlGaAs layer was grown using a different aluminum beam flux. Cleavage along a plane perpendicular to the substrate surface (usually (110) or $(1\bar{1}0)$ planes) and etching showed a good contrast in SEM images taken

from cross-sectional areas of the heterostructure but did not permit thickness measurements with good accuracy.

A more precise method can be employed to determine composition by band gap determination using photoluminescence analysis. The $\text{Al}_x\text{Ga}_{1-x}\text{As}$ band gap measured at room temperature is related to x by the expression [50]:

$$E_g = 1.414 + 1.266x + 0.266x^2. \quad (3.5)$$

A series of four structures was grown to determine precisely the relationship between gallium/aluminum beam flux ratio and x . All structures consisted of a GaAs substrate, a $0.5 \mu\text{m}$ thick undoped GaAs buffer layer and $\approx 1.0 \mu\text{m}$ of undoped $\text{Al}_x\text{Ga}_{1-x}\text{As}$ with x ranging from about 0.1 to 0.4. The substrate temperature was kept at 600°C during growth. It was observed that the RHEED pattern remained the same for GaAs growth and $\text{Al}_x\text{Ga}_{1-x}\text{As}$ for small values of x but tended to be spot-like and the surface reconstruction pattern was not so evident for larger x values ($x > 0.2$).

Photoluminescence analysis in this set of samples provided the band gap which was used to calculate the x value for each $\text{Al}_x\text{Ga}_{1-x}\text{As}$ layer. Table 3.4 presents Ga and Al beam fluxes used for each sample as well the band gap and x value obtained from the band gap using equation 3.5. Using this x value it is possible to calculate the aluminum beam flux for a given gallium beam flux and any x . Using the fact that

$$GR(GaAs) = BEP(Ga) \times K_{Ga},$$

$$GR(AlAs) = BEP(Al) \times K_{Al},$$
(3.6)

where K_{Ga} and K_{Al} are constants which incorporate the relative ion gauge sensitivities for each element, it is possible to write equation (3.4) in a more appropriate way:

$$x = \frac{BEP(Al) \times K_{Al}}{BEP(Al) \times K_{Al} + BEP(Ga) \times K_{Ga}} =$$
(3.7)

$$= \frac{BEP(Al)}{BEP(Al) + K \times BEP(Ga)},$$

where $K = K_{Ga}/K_{Al}$, the ion gauge sensitivity ratio, was determined from the data in Table 3.4.

Table 3.4 Growth parameters, room temperature band gap and x values for a series of $Al_xGa_{1-x}As$ layers

BEP (Ga) (10^{-7} torr)	BEP (Al) (10^{-8} torr)	band gap (eV)	x
5.10	9.10	1.77	0.266
5.15	5.95	1.67	0.194
5.14	3.79	1.59	0.135
5.29	1.51	1.49	0.059

Finally, equation (3.7) can be written in a different form, using $K = 0.49$, which permits to obtain the aluminum

beam flux for a given x , as a function of the gallium beam flux:

$$BEP(Al) = 0.49 \times BEP(Ga) \times \frac{x}{(1-x)}. \quad (3.8)$$

The growth rate of the ternary compound is given by

$$\begin{aligned} GR &= \frac{BEP(Ga)}{4.7 \times 10^{-7} \text{ torr}} + \frac{BEP(Al)}{2.31 \times 10^{-7} \text{ torr}} = \\ &= \frac{BEP(Ga)}{(4.7 \times 10^{-7} \text{ torr}) \times (1-x)} \quad [\mu\text{mhr}^{-1}]. \end{aligned} \quad (3.9)$$

Doping levels in n-type and p-type AlGaAs were determined by measuring resistivity and Hall voltage in Si-doped and Be-doped AlGaAs layers, respectively. The first measurements showed that it was not trivial to obtain ohmic contacts on AlGaAs. Some methods used comprise:

(i) application of indium dots onto the substrate surface followed by sample heating in reducing atmosphere (this method worked very well for doped GaAs layers);

(ii) surface etching with HCl for 2 minutes at room temperature to remove the oxide layer followed by deposition of 2000 Å-thick Au-Ge contacts and heating at 450°C for 5 minutes in reducing atmosphere;

(iii) growth of an undoped 50 Å-thick GaAs cap layer on AlGaAs followed by melting of indium dots in a similar manner employed for making contacts on GaAs.

The last method improved dramatically the contact quality. AlGaAs surfaces, in contact with air, easily form a stable insulating oxide layer which prevents the formation of good ohmic contacts. The 50 Å-thick undoped GaAs layer seems to be sufficient to prevent oxidation of the underlayer. Nevertheless, it is still possible to diffuse indium from the top surface through the protective GaAs layer until it reaches the doped AlGaAs layer which had not been exposed to atmosphere. In fact, Drummond et al. [51] grew a 200 Å thick undoped GaAs cap layer after growth of a 1.0 - 1.5 μm thick Si-doped $\text{Al}_{0.25}\text{Ga}_{0.75}\text{As}$ obtaining similar results. Figure 3.5

50 Å undoped GaAs
2 μm doped AlGaAs
0.5 μm undoped AlGaAs
0.5 μm undoped GaAs
semi-insulating GaAs substrate

Figure 3.5 AlGaAs/GaAs structures grown by MBE for electrical measurements

presents the structures grown for electrical measurements. Two different x values were chosen for the $\text{Al}_x\text{Ga}_{1-x}\text{As}$ layers, namely 0.2 and 0.3 as these two compositions are frequently employed in optoelectronic devices. A reasonable estimate can be obtained from these values for other compositions. To determine which temperature would lead to better electronic properties, some structures were grown at two different temperatures although the best temperature for electronic properties does not necessarily indicate the temperature of choice to grow structures for application in optoelectronic devices. Table 3.5 presents the results obtained from Hall-effect measurements. It was observed that there was a decrease in electron concentration when a higher substrate temperature (700°C) was employed during growth of the AlGaAs layer.

The electrical measurements showed there is a spreading of data for AlGaAs , which agrees with the results of Collins et al. [52], in contrast with the results obtained for GaAs . For instance, at a given substrate temperature and constant x , the electron concentration was significantly different for the same silicon source temperature. This is due mainly to different background conditions in the growth chamber as those structures were grown in different occasions. For Be-doped samples the AlGaAs layers seemed not to be so sensitive to the growth chamber environment. It has been observed that the quality of AlGaAs layers is particularly sensitive to impurities and a high background pressure [53].

Table 3.5 Electronic properties of Si-doped and Be-doped $\text{Al}_x\text{Ga}_{1-x}\text{As}$ layers grown by MBE

T_{Si}	T_{ss}	x	μ	n	ρ
1230	700	0.30	396	8.9 E16	1.8 E-1
1280	700	0.30	502	1.2 E17	1.1 E-1
1330	700	0.30	341	1.3 E17	1.1 E-1
1280	650	0.30	507	2.7 E17	4.6 E-2
1330	650	0.30	357	3.4 E17	5.1 E-2
1250	650	0.30	714	5.5 E17	1.6 E-2
1280	650	0.30	657	7.0 E17	1.4 E-2
1310	650	0.30	426	1.1 E18	1.4 E-2
1250	650	0.20	1084	1.0 E18	5.7 E-3
1280	650	0.20	908	1.5 E18	4.6 E-3
1310	650	0.20	714	2.5 E18	3.6 E-3

T_{Be}	T_{ss}	x	μ	p	ρ
850	700	0.3	134	2.4 E17	1.9 E-1
850	650	0.3	123	5.4 E17	9.4 E-2
920	650	0.3	50	9.6 E18	1.3 E-2
820	650	0.2	115	4.6 E17	1.1 E-1
860	650	0.2	80	2.2 E18	3.7 E-2
900	650	0.2	56	9.1 E18	3.5 E-2

$T_{\text{Si}}, T_{\text{Be}}$ = source temperature ($^{\circ}\text{C}$);
 T_{ss} = substrate temperature ($^{\circ}\text{C}$);
x = AlGaAs composition;
 μ = electron mobility ($\text{cm}^2 \text{V}^{-1} \text{s}^{-1}$);
n, p = carrier concentration (cm^{-3});
 ρ = resistivity (Ωcm);
measurements made at 300 K.

The carrier mobilities of AlGaAs layers grown after bake-out of the MBE chambers were unusually low compared with samples grown a few weeks afterwards when the background pressure was lower. Furthermore, high electron concentrations in AlGaAs are not easily obtained. When a higher electron concentration is pursued by increasing the silicon source temperature, a larger compensation ratio is present and effective carrier concentration as well mobility drops sharply. This fact is consistent with the results of Drummond et al. [51]. In addition, it was observed that excessive silicon doping induces the formation of dislocation loops in AlGaAs as observed in cross-sectional transmission electron microscopy (X-TEM) at high Si-doping levels (higher than 10^{18} cm^{-3}). For Be-doped layers this problem was not observed and relatively high carrier concentrations were easily obtained. The hole mobility at room temperature compares fairly well with the results of Collins et al. [52].

It was found that when aluminum content was increased, i.e., when x was changed from 0.2 to 0.3, both electron and hole concentrations decreased significantly, as can be seen in figures 3.6 and 3.7, for the same dopant source temperatures. This indicates that the decrease in free carriers is caused by a change in the behavior of Si and Be dopant atoms, since Si and Be concentrations in the epitaxial layer were kept nearly constant. Salmon and D'Haenens [54] studied the effect of aluminum composition on silicon behavior in $\text{Al}_x\text{Ga}_{1-x}\text{As}$ and found

that there was no significant variation of the total Si concentration, measured by SIMS, when the aluminum content was increased, although carrier concentration dropped sharply as x increased.

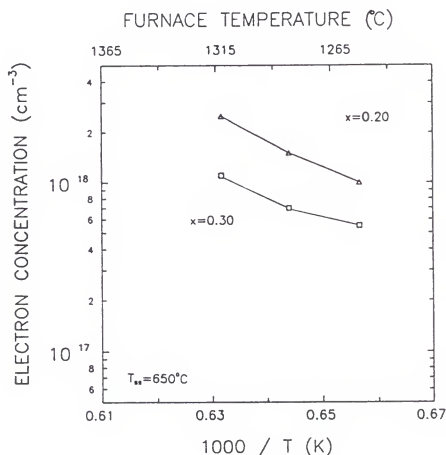


Figure 3.6 Electron concentration of Si-doped $\text{Al}_x\text{Ga}_{1-x}\text{As}$ layers as a function of silicon source temperature for two values of x , namely 0.2 and 0.3.

In the present work, it was found that electron Hall mobility decreased significantly when x was increased from 0.2 to 0.3, a result which agrees with the literature mentioned above.

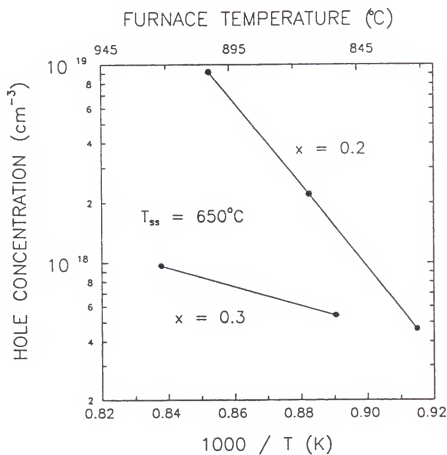


Figure 3.7 Carrier concentration of Be-doped $\text{Al}_x\text{Ga}_{1-x}\text{As}$ layers as a function of beryllium source temperature for two values of x , namely 0.2 and 0.3.

Conclusions

The substrate preparation procedures were reported in this chapter. No chemical etching was used in this work since the uv/ozone exposure technique followed by in-situ oxide desorption showed to provide adequate substrate growth surface.

Electrical measurements performed in GaAs epilayers revealed good agreement between the experimental data and theoretical predictions based on the dopant incorporation rate. These data also agreed with results reported in the literature. For n-doped layers, the electron mobility versus electron concentration curves indicated a compensation ratio around 2, which indicates a material of good purity.

In AlGaAs layers grown on GaAs substrates, the approach employed to calculate the layer composition based on Ga/Al flux ratio revealed to be quite acceptable when compared to composition determined by band gap determination.

Electrical measurements of Si-doped AlGaAs layers showed these layers to be quite sensitive to the background environment. Be-doped samples did not show a significant dependence on the environment. Furthermore, a clear dependence of carrier concentration on aluminum content was evident when layers with $x = 0.2$ and 0.3 were compared. Both p-type and n-type layers presented lower carrier concentrations for higher aluminum contents, in agreement with earlier works.

CHAPTER 4
GROWTH AND CHARACTERIZATION OF
 $\text{In}_x\text{Ga}_{1-x}\text{As}/\text{GaAs}$ HETEROSTRUCTURES

In this chapter, the growth and characterization of $\text{In}_x\text{Ga}_{1-x}\text{As}/\text{GaAs}$ epitaxial layers having a wide range of compositions will be reported. Initially, $\text{In}_x\text{Ga}_{1-x}\text{As}$ layers were grown with different compositions in order to study:

- (i) the composition and growth rate dependence on gallium and indium beam flux levels;
- (ii) the composition and growth rate dependence on substrate temperature;
- (iii) the epilayer quality as a function of composition and substrate temperature;
- (iv) the strain relief mechanisms occurring in the $\text{In}_x\text{Ga}_{1-x}\text{As}/\text{GaAs}$ system.

Four sets of samples, each set with a different composition, were grown under the following conditions (see Table 4.1):

- the gallium beam equivalent pressure was maintained constant for all samples, $\text{BEP (Ga)} = 4.7 \times 10^{-7}$ Torr;
- the indium beam equivalent pressure was maintained constant within each set of samples but changed from one group to another to provide a different indium content (x);

- the arsenic beam equivalent pressure was kept constant during growth of each set of samples and made equal to nearly sixteen times the sum of gallium and indium BEP;

- all $\text{In}_x\text{Ga}_{1-x}\text{As}$ layers were grown on a $0.1\ \mu\text{m}$ thick undoped GaAs buffer layer grown at 600°C on a semi-insulating (001) GaAs substrate;

- the substrate temperature varied from growth to growth in the range of 400°C to 560°C .

Table 4.1 Growth conditions for $\text{In}_x\text{Ga}_{1-x}\text{As}$ epitaxial layers grown on GaAs substrates.

x	$T_{ss}\ (^{\circ}\text{C})$	BEP (In) (10^{-7} torr)	BEP (As) (10^{-6} torr)	GR ($\text{\AA}\text{sec}^{-1}$)
0.05	440-480-520-560	0.50	8.5	2.26
0.12	440-480-520-560	1.16	9.7	2.59
0.18	400-440-480-520	1.98	10.2	2.74
0.26	400-440-480-520	3.06	12.7	3.35

x = In content obtained by microprobe analysis

T_{ss} = substrate temperature

BEP = beam equivalent pressure

GR = growth rate measured with a Dektak II-A profilometer

Composition Analysis

Composition analysis was carried out using four different techniques. The method described in Chapter 3, based on the band gap measurement by photoluminescence analysis and used to determine AlGaAs layers composition does not apply for

InGaAs layers since another variable is introduced for this material, namely, the strain effect which causes a shift in the band gap. A few other methods may be used but all of them have limitations so that absolute numbers are difficult to obtain although comparative results are possible:

(a) Epilayer thickness measurements using cross-sectional transmission electron microscopy (XTEM) or step measurement with a profilometer provides the growth rate in the [001] direction which is not necessarily related to composition unless it is assumed there is a complete relaxation of the InGaAs layer which seldom occurs. If InGaAs thickness is measured and GaAs growth rate is known, the InAs growth rate is given by the difference between the ternary compound and GaAs growth rates,

$$GR(InAs) = GR(InGaAs) - GR(GaAs) . \quad (4.1)$$

As the lattice parameter of InAs is equal to 6.058 Å and that of GaAs is 5.654 Å, for the same thickness there will be $5.654/6.058 = 0.9333$ indium atoms for each gallium atom. Thus,

$$x = \frac{0.9333 GR(InAs)}{0.9333 GR(InAs) + GR(GaAs)} . \quad (4.2)$$

This method may provide an estimate for x value but is not accurate because it incorporates two errors, the first being the thickness measurement error and the second, the assumption that there is complete relaxation.

(b) Determination of composition from lattice parameter measurement by X-ray diffraction analysis would give very precise results if either the residual strain in the epilayer was known or a complete relaxation occurred. It was found that even for thick InGaAs layers grown directly on GaAs complete relaxation does not occur, thus X-ray diffraction analysis gives only an estimate of the composition.

(c) Photoluminescence as well as absorption analyses are methods which provide very accurate band gap measurements. The energy gap is a function of composition in ternary compounds and data is available for unstrained materials [55]. Nevertheless, the residual strain causes a shift in the band gap difficult to assess independently if composition is not known.

(d) Electron microprobe analysis is an alternative method which works independently of both the strain state and lattice parameter of the material. In order to obtain absolute values in atomic percentage, standard samples must be provided to calibrate the equipment. This was the method of choice in this work. GaAs, InAs, and $\text{In}_{0.53}\text{Ga}_{0.47}\text{As}$ standard samples of known compositions were used before each measurement was carried out. A composition cross-check was possible by comparing the figures obtained with this analysis and the other methods mentioned above particularly X-ray diffraction, photoluminescence, and absorption.

The x value of a layer can be obtained as a function of gallium and indium beam equivalent pressures (BEP) as

$$x = \frac{BEP(In)}{BEP(In) + 1.50 BEP(Ga)} , \quad (4.3)$$

where the factor 1.50 is the relative ion gauge sensitivity for indium and gallium, determined experimentally from the beam equivalent pressure of these two elements in epitaxial layers where the chemical composition was determined using an electron microprobe.

If a particular composition is pursued, the indium beam equivalent pressure may be given as a function of gallium BEP:

$$BEP(In) = 1.50 \times BEP(Ga) \times \frac{x}{(1-x)} . \quad (4.4)$$

The InGaAs growth rate was determined by measuring film thicknesses of partially masked samples using a Dektak II-A profilometer in addition to measuring film thicknesses via cross-sectional TEM images. The growth rate as a function of indium and gallium beam equivalent pressures is given by

$$\begin{aligned} GR(InGaAs) &= \frac{BEP(In)}{5.48 \times 10^{-7} \text{ torr}} + \frac{BEP(Ga)}{4.70 \times 10^{-7} \text{ torr}} \quad [\mu\text{m hr}^{-1}] \\ \text{or} \quad &= \frac{BEP(In)}{1.97 \times 10^{-7} \text{ torr}} + \frac{BEP(Ga)}{1.69 \times 10^{-7} \text{ torr}} \quad [\text{\AA sec}^{-1}] . \end{aligned} \quad (4.5)$$

Determination of Residual Strain in $\text{In}_x\text{Ga}_{1-x}\text{As/GaAs}$ Layers

Whenever heteroepitaxy takes place, the lattice mismatch between the epilayer and substrate can be accommodated either by elastic strain or by generation of misfit dislocations or a combination of the two. Dislocations can be confined in the heterointerface or propagate in a threading manner through either the epilayer or the substrate. For epitaxial layers thinner than the so-called critical thickness [24-27], the material will remain in an elastically strained state. If the epilayer is thicker than the critical value, most of the mismatch is accommodated via dislocation generation although residual strain can still be present [13,56]. In this work, the residual strain in thick $\text{In}_x\text{Ga}_{1-x}\text{As/GaAs}$ layers was determined by X-ray analysis.

In a cubic crystal of lattice parameter a , the interplanar distance is given by

$$d = \frac{a}{\sqrt{h^2 + k^2 + l^2}}, \quad (4.6)$$

where h , k , and l are the Miller indices of the plane. For zinc-blende structures, diffraction occurs when h , k , and l are unmixed (either all even or all odd numbers).

Thus, the (004) plane will be seen, according to Bragg's law, at an angle 2θ given by

$$\sin\theta = \frac{n\lambda}{2d} = \frac{2\lambda}{a}. \quad (4.7)$$

Therefore, if a copper crystal with X-ray wavelength $K_{\alpha 1} = 1.5406 \text{ \AA}$ and $K_{\alpha 2} = 1.5444 \text{ \AA}$ is used, 2θ for GaAs will be equal to 66.044° . Table 4.2 presents lattice parameter, interplanar distance and angle 2θ for the binary compounds of interest.

A completely relaxed ternary compound will have a lattice parameter with an intermediate value between the lattice parameters of the binary compounds. If it is assumed that this value obeys a linear interpolation, the lattice parameter of a relaxed ternary compound can be given by an expression of the form

$$a_r(\text{In}_x\text{Ga}_{1-x}\text{As}) = a(\text{GaAs}) + \Delta a \times x, \quad (4.8)$$

where $\Delta a = a(\text{InAs}) - a(\text{GaAs}) = 0.404 \text{ \AA}$ (see Table 4.2).

Table 4.2 Lattice parameter, (400) interplanar distance, and angle of the corresponding X-ray beam for binary compounds.

Compound	a (Å)	d_{400} (Å)	2θ (°)
GaAs	5.654	1.4135	66.044
InAs	6.058	1.5145	61.143
AlAs	5.660	1.4150	65.965

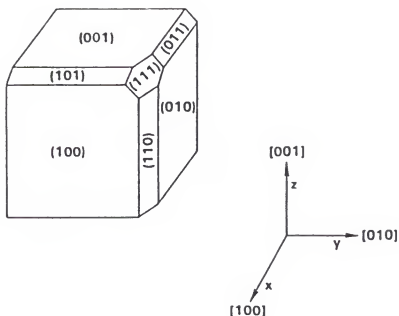


Figure 4.1 Major crystallographic planes and directions in a cubic lattice.

At the other extreme, a completely strained layer grown on GaAs will have a tetragonal lattice with $a_x = a_y = a(\text{GaAs})$ or simply a , where a_x and a_y are the cell lattice parameters contained in the (001) growth plane, as shown in Figure 4.1. The lattice parameter a_z , perpendicular to the (001) plane, may be calculated by

$$V = a_r^3 = a^2 \times a_z ,$$

$$a_z = \frac{(a + 0.404x)^3}{a^2} \quad (4.9)$$

assuming that the volume of the cubic crystal (relaxed ternary compound) is the same as the volume of the tetragonal distorted crystal (strained ternary compound).

Another assumption is that all of the strain is accommodated in the ternary compound layer with the GaAs remaining essentially strain-free, although this is not always true, particularly for more complex structures such as strained-layer superlattices or multi-stage structures.

If a partial relaxation occurs in such a ternary layer, the residual strain can be calculated by obtaining the lattice parameter in the growth direction [001], a_{meas} , from the X-ray diffraction pattern:

$$a_{meas} = a + \Delta d \times 4, \quad (4.10)$$

$$\Delta d = \frac{\lambda}{2} \left(\frac{1}{\sin\theta(InGaAs)} - \frac{1}{\sin\theta(GaAs)} \right),$$

thus,

$$residual\ strain\ (\%) = \frac{a_{meas} - a_r}{a_z - a_r} \times 100\ \%. \quad (4.11)$$

Thick $In_xGa_{1-x}As$ layers ($t > 1\ \mu m$) grown on GaAs substrates were found to have residual strain according to the results obtained from X-ray diffraction data presented in Table 4.3. An InAs layer grown on GaAs was included for comparison. The x values were obtained from electron microprobe analysis.

The residual strain was different for each layer depending on its indium content. It was found that higher indium contents induced higher degrees of relaxation. This phenomenon may be linked to two factors: (i) the driving force to begin relaxation is proportionally higher for higher indium contents and (ii) the relaxation mechanism itself is different for high indium content layers as will be discussed in the structural analysis section at the end of this chapter. Typical X-ray diffraction patterns obtained from thick InGaAs/GaAs layers are presented in Figure 4.2 and Figure 4.3.

Table 4.3 Lattice parameters and residual strain of $\text{In}_x\text{Ga}_{1-x}\text{As}$ epitaxial layers grown on GaAs substrates.

x	a_r (Å)	a_z (Å)	a_{meas} (Å)	residual strain (%)
0.05	5.674	5.714	5.692	20.6
0.12	5.704	5.804	5.712	8.3
0.18	5.728	5.880	5.738	6.4
0.26	5.761	5.981	5.769	3.6
0.37	5.804	6.117	5.813	2.9
1.00	6.058	6.955	6.065	0.8

x = composition measured from microprobe analysis
 a_r = lattice parameter of relaxed $\text{In}_x\text{Ga}_{1-x}\text{As}$
 a_z = lattice parameter of strained $\text{In}_x\text{Ga}_{1-x}\text{As}$
 a_{meas} = lattice parameter of the epilayer, measured by X-ray diffraction analysis

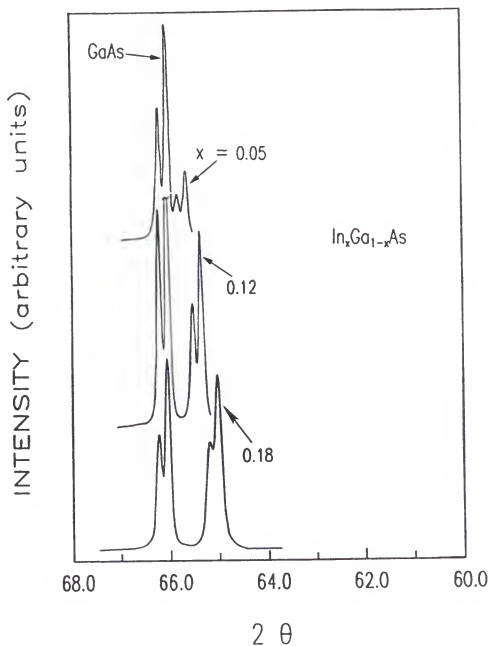


Figure 4.2 X-ray diffraction patterns observed for $1\text{ }\mu\text{m}$ thick InGaAs epilayers grown on GaAs substrates.

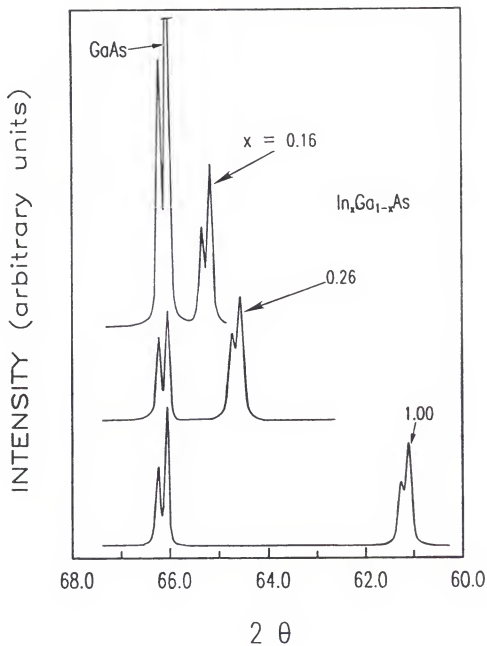


Figure 4.3 X-ray diffraction patterns observed for 1 μm thick InGaAs epilayers grown on GaAs substrates.

Identification of Strain Relief Mechanisms

One of the reasons why thick InGaAs layers were grown on GaAs substrates was to investigate strain relief in the $\text{In}_x\text{Ga}_{1-x}\text{As}/\text{GaAs}$ system, which occurs whenever the epilayer thickness is greater than a critical value. The $\text{In}_x\text{Ga}_{1-x}\text{As}$ composition ranged in this study from $x = 0.05$ to $x = 0.49$. In order to fully characterize this range, a few more samples were grown in addition to the layers described in Table 4.1. The growth conditions for these additional layers are presented in Table 4.4. The gallium beam equivalent pressure was kept constant and equal to 4.6×10^{-7} Torr.

Table 4.4 Conditions during growth of low and high indium content $\text{In}_x\text{Ga}_{1-x}\text{As}$ single layers.

x	T_{ss} ($^{\circ}\text{C}$)	BEP (In) (10^{-7} torr)	BEP (As) (10^{-6} torr)	GR (\AA sec^{-1})
0.14	500	1.16	9.4	3.37
0.16	500	1.34	9.7	3.47
0.37	440	3.95	13.7	4.80
0.49	440	6.54	15.3	6.13

x = In content obtained by electron microprobe analysis

T_{ss} = substrate temperature

BEP = beam equivalent pressure

GR = growth rate

In all samples, the $\text{In}_x\text{Ga}_{1-x}\text{As}$ layer was much thicker than the critical value necessary to start lattice relaxation so that a strain relief process was expected to occur. Cross-sectional (XTEM) and planar (PTM) transmission electron microscopy analyses were conducted in a JEOL 200CX transmission electron microscope to investigate the relaxation mechanisms. The specimens for XTEM were prepared by a mechanical polishing process to a thickness of $\approx 50 \mu\text{m}$ followed by Ar^+ ion milling at room temperature. PTM samples were prepared by chemical etching in a bromine-methanol solution.

It was found that the strain relief processes are different for each range of compositions according to the following categories:

$x = 0.05 - 0.16$	small x layers
$x = 0.18 - 0.28$	medium x layers
$x = 0.37 - 0.50$	large x layers

XTEM analysis of small x samples showed an absence of threading dislocations in the InGaAs layers, however, dislocations were observed at the InGaAs/GaAs interface (Figure 4.4). Many of these dislocations appear to propagate in the GaAs material as shown in Figure 4.5. Analysis of medium x layers revealed the presence of threading dislocations in the InGaAs layers as well as at the InGaAs/GaAs interface (Figure 4.6). A high dislocation density

was observed in large x layers (Figure 4.7), however, there appears to be an absence of dislocations in the GaAs material.

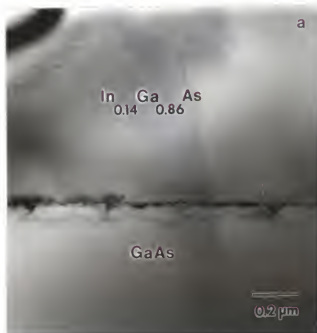


Figure 4.4 InGaAs/GaAs interface showing absence of dislocations in the InGaAs layer and dislocations generated at the interface.

In samples with small x layers, dislocations nucleate at the InGaAs/GaAs interface and propagate into the GaAs due to the fact that GaAs has a smaller shear modulus than InGaAs. The few dislocations which manage to propagate into the InGaAs epilayer experience biaxial in-plane compressive stresses since the epilayer has a larger lattice parameter than the

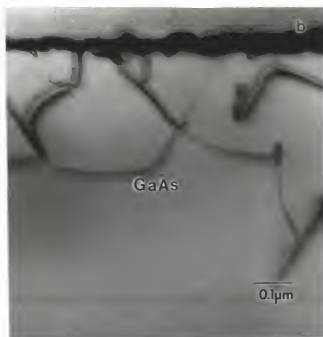


Figure 4.5 GaAs buffer layer in a InGaAs/GaAs heterostructure presenting dislocations generated and propagated from the interface ($x = 0.12$).

substrate and, as a consequence, are bent away from the surface towards the edges of the specimen.

Dislocations in medium x layers appear to nucleate at both the InGaAs/GaAs interface and the free surface. Surface nucleation of dislocations is observed in Figure 4.8. GaAs will yield first due to its smaller shear modulus which explains the presence of dislocations in the GaAs material, however, strain relief due to GaAs plastic deformation is insufficient to offset the increase in strain due to



Figure 4.6 $\text{In}_{0.21}\text{Ga}_{0.79}\text{As}$ ($x \approx 0.2$) layer showing dislocations originated from both the InGaAs/GaAs interface and growth surface.

increasing thickness of the InGaAs epilayer as growth proceeds. Thus, a critical stress is reached at which point dislocations can nucleate at the free surface. Consequently, strain relief in medium x layers is due partially to both the plastic deformation of GaAs and the presence of threading dislocations in the InGaAs epilayer.

In large x layers, dislocations appear to nucleate mainly at the surface. During the initial stages of growth, a few dislocations may nucleate at the interface, however, these

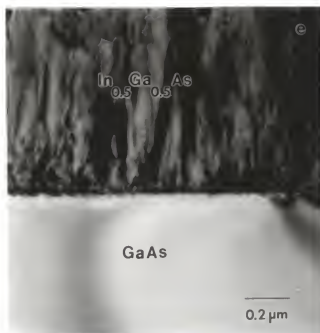


Figure 4.7 $\text{In}_{0.5}\text{Ga}_{0.5}\text{As}$ epilayer grown on GaAs, presenting a high dislocation density originated mostly at the free surface.

dislocations would experience strong surface image forces due to the small critical thickness associated with large x layers and would thus propagate to the growth surface. This phenomenon would explain the absence of dislocations in the GaAs material. As epilayer thickness increases during growth, the critical stress for surface dislocation nucleation will be reached, resulting in the downward propagation of threading dislocations originated at the growth surface. Hence, in large x layers, strain relief occurs mainly due to the formation of threading dislocations in the InGaAs material.

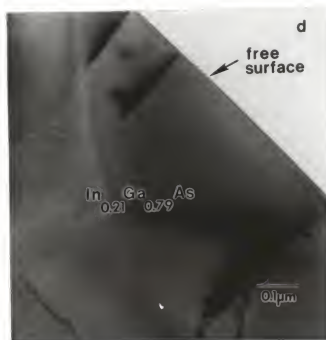


Figure 4.8 Thick $\text{In}_x\text{Ga}_{1-x}\text{As}$ layer showing some dislocations nucleated at the free surface and propagating through the epilayer ($x \approx 0.2$).

It is appropriate to introduce here a new concept, which we define as "critical composition", based on the understanding of the strain relief processes previously described. The "critical composition" may be defined as the x value at which dislocations nucleate at the free surface. This composition was found to be between $x = 0.16$ and $x = 0.18$. Below the critical composition it may be possible to obtain threading dislocation-free thick InGaAs layers on GaAs. This

phenomenon may be unique to the InGaAs/GaAs system since it has not been reported for any other heteroepitaxial system.

The samples which presented no dislocations in XTEM analysis were studied in PTEM to determine dislocation density. A relatively low magnification was used to cover the largest possible area each time a sample region was studied. A simple calculation can provide the dislocation density as a function of the number of counted dislocations per unit area. The dislocation density may be given by

$$\rho = \frac{NM^2}{80n} \quad [cm^{-2}], \quad (4.12)$$

where M is the image magnification, n is the number of analyzed frames with an area of $8 \times 10^4 \text{ cm}^2$, and N is the total number of dislocations counted over all frames. For a magnification equal to 3×10^4 , and 50 analyzed frames, the lowest dislocation density which can be counted is $2 \times 10^5 \text{ cm}^{-2}$, thus for samples which did not present any dislocation during this analysis it is assumed the dislocation density is less than $2 \times 10^5 \text{ cm}^{-2}$.

$\text{In}_x\text{Ga}_{1-x}\text{As/GaAs}$ layers with $x \leq 0.16$ presented dislocation densities lower than the measurable value in PTEM analysis, $2 \times 10^5 \text{ cm}^{-2}$. Samples with $x > 0.16$ were not measured in PTEM as a reasonable number were detected in XTEM analysis.

Photoluminescence and Absorption Analyses
of $\text{In}_x\text{Ga}_{1-x}\text{As/GaAs}$ Layers

$\text{In}_x\text{Ga}_{1-x}\text{As/GaAs}$ layers with $x = 0.05$ and 0.12 were analyzed with an Ar^+ laser, with $\lambda = 5145 \text{ \AA}$ and power output of 100 mW . Transmitted or emitted light was focused onto the entrance of a 1.26 m focal length Spex grating spectrometer. The detector was an EG&G type HUV-1100 Si photodiode. Photoluminescence and absorption analyses were performed at room temperature. These layers presented a weak photoluminescence.

For $x = 0.05$, four samples grown at different substrate temperatures, with all other growth conditions kept constant, were studied in order to determine the photoluminescence dependence with substrate temperature. The collected data are presented in Table 4.5. As was expected, no dependence of photoluminescence or absorption characteristic wavelength with substrate growth temperature was observed. Photoluminescence intensity, however, did change when substrate temperature was varied. Higher intensity photoluminescence peaks were observed for higher substrate growth temperatures in the studied range. Stronger PL signal was related in earlier works to higher quality epitaxial layers [57]. It has been observed that a higher substrate temperature during growth improves the photoluminescence intensities particularly for layers with carrier concentrations below 10^{18} cm^{-3} in GaAs [9]. Some values obtained

from equations found in the literature [55,58], which provide the band gap of unstrained $\text{In}_x\text{Ga}_{1-x}\text{As}$ layers as a function of x , are included in Table 4.5 for comparison. The results obtained in this work showed a nearly constant wavelength for this range of compositions, accounting for a good growth reproducibility.

Table 4.5 Photoluminescence and absorption data obtained from $\text{In}_x\text{Ga}_{1-x}\text{As}/\text{GaAs}$ layers, where the In content, x , was measured by electron microprobe.

x	T_{ss} ($^{\circ}\text{C}$)	Photoluminescence		Absorption	
		peak (nm)	E_g (eV)	edge (nm)	E_g (eV)
0.05	440	924	1.341	923	1.34
0.05	480	921	1.346	922	1.34
0.05	520	923	1.343	923	1.34
0.05	560	923	1.344	923	1.34
0.05	[55]	923	1.343	-	-
	[58]	916	1.353	-	-

Absorption analysis was performed on a comparative basis. The absorption, in arbitrary units, is given by

$$A = \log\left(\frac{1}{T}\right), \quad (4.13)$$

where T is equal to I_t/I_0 , the ratio between the intensity of transmitted and incident light.

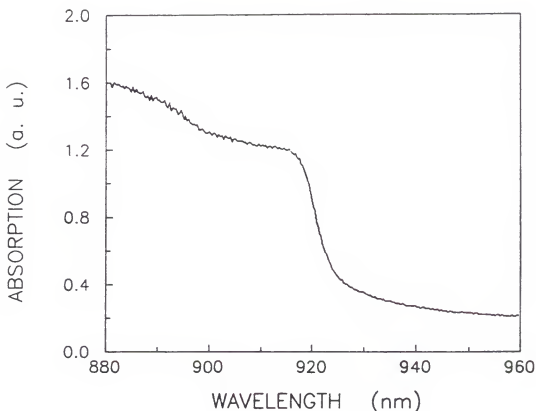


Figure 4.9 Absorption spectra of an $\text{In}_{0.05}\text{Ga}_{0.95}\text{As}$ layer. The second edge at left (≈ 895 nm) corresponds to GaAs substrate absorption.

Absorption spectra showed a very good agreement with photoluminescence data. Two absorption edges were seen. The first, observed at a shorter wavelength, corresponds to the GaAs substrate absorption (≈ 890 nm). The second absorption edge corresponds to the $\text{In}_x\text{Ga}_{1-x}\text{As}$ layer. Figure 4.9 shows a typical absorption spectrum for an $\text{In}_{0.05}\text{Ga}_{0.95}\text{As}$ layer. The

relatively steep curve accounts for layers of good quality presenting a low number of shallow recombination centers.

Table 4.6 Absorption data obtained from analysis of $\text{In}_x\text{Ga}_{1-x}\text{As}/\text{GaAs}$ layers. The indium content, x was measured by electron microprobe.

x	T_{ss} ($^{\circ}\text{C}$)	Absorption	
		edge (nm)	E_g (eV)
0.12	440	999	1.24
0.12	480	993	1.25
0.12	520	984	1.26
0.13	560	1000	1.24
0.12	[55]	1008	1.23
	[58]	994	1.25

The photoluminescence results obtained from $\text{In}_x\text{Ga}_{1-x}\text{As}$ layers with $x = 0.12$ or higher are not included in this work since the Si photodetector upper limit was close to the photoluminescence peaks observed and the peaks could not be resolved well from the background. Nevertheless, absorption analysis showed a good agreement between the band gaps found in the literature and the results presented in this work (Table 4.6).

Comparison between theoretical calculations for the unstrained band gap and photoluminescence and absorption

analysis permitted a more complete examination of the strain state and quality of InGaAs epitaxial layers. It was expected that some strain would remain in thick InGaAs layers, which was indeed found by X-ray diffraction analysis in the epilayers subject of this study. Nevertheless, comparison with the theoretical band gap of unstrained materials did not show a significant difference. This discrepancy may be due to the fact that the residual strain present in the epitaxial layers was not enough to cause a detectable shift in the band gap. Another reason could be the use of different methods for measuring $\text{In}_x\text{Ga}_{1-x}\text{As}$ composition or theory not well fitted for this particular composition range, as can be observed if the band gaps calculated for the same composition ($x = 0.05$) from different works [55,58] are compared.

Conclusions

Thick $\text{In}_x\text{Ga}_{1-x}\text{As}$ layers ($t > 1 \mu\text{m}$) with compositions ranging from $x = 0.05$ to 0.50 were grown on (001) GaAs substrates by molecular beam epitaxy, such that in all cases the epilayer thickness was much greater than the critical thickness.

Several methods were employed to characterize the epitaxial layers. X-ray diffraction analysis showed there was some residual strain in the $\text{In}_x\text{Ga}_{1-x}\text{As}$ layers. For higher indium

content, the residual strain was smaller, indicating that the strain relaxation processes were composition dependent.

Cross-sectional and planar TEM revealed that there are different strain relief processes depending on the composition range being considered. For layers with $x < 0.16$, the strain is relieved mostly at the InGaAs/GaAs interface, the InGaAs layer remaining essentially dislocation-free. For larger x up to ≈ 0.28 , there is a mixed process, with dislocations being generated at either the interface or the free surface. In larger x layers, dislocations are generated mostly at the free surface.

Photoluminescence and absorption measurements in low x $\text{In}_x\text{Ga}_{1-x}\text{As}$ layers showed good material quality. Comparison to band gap theoretical predictions for unstrained layers revealed those layers are close to an unstrained state. The constant PL peaks and absorption edges obtained at different substrate growth temperatures indicate that indium incorporation rate did not change for the substrate growth temperature range employed and a good reproducibility is obtained for samples grown under the same conditions.

The concept of "critical composition" was introduced and defined as the composition at which dislocations nucleate at the epilayer free surface. This composition was found to be between $x = 0.16$ and 0.18 for $\text{In}_x\text{Ga}_{1-x}\text{As}$ epitaxial layers. For thick $\text{In}_x\text{Ga}_{1-x}\text{As}$ layers with x smaller than 0.16 , misfit

dislocations generate at the InGaAs/GaAs interface will not propagate into the $\text{In}_x\text{Ga}_{1-x}\text{As}$ layers.

The findings of this chapter suggest that $\text{In}_x\text{Ga}_{1-x}\text{As}$ epitaxial layers with $x < 0.16$ may serve as buffers for growing lattice-matched structures to be employed in optoelectronic devices, since an acceptable structural defect level and good photoluminescence and absorption characteristics indicate these layers have a satisfactory quality. Furthermore, these low indium content $\text{In}_x\text{Ga}_{1-x}\text{As}/\text{GaAs}$ layers can be employed as the first stage in multi-stage buffer systems to be utilized for growing $\text{In}_x\text{Ga}_{1-x}\text{As}$ layers with high indium content, e.g., $x = 0.4$ or 0.5 , as will be demonstrated later in this work.

CHAPTER 5
GROWTH OF OPTOELECTRONIC DEVICE-QUALITY $\text{In}_{0.4}\text{Ga}_{0.6}\text{As}$

Introduction

Growth of high indium content $\text{In}_x\text{Ga}_{1-x}\text{As}$ layers on GaAs substrates presents a serious problem when high quality dislocation-free material is to be grown. As demonstrated in the previous chapters, low indium content ($x < 0.16$) single layers can be successfully grown directly on GaAs, the misfit dislocations due to lattice mismatch being confined mostly at the heterointerface with some of these dislocations propagating into the GaAs buffer layer. Higher indium content (x up to ≈ 0.3) layers can be grown dislocation-free as part of strained-layer superlattices (SLSs). However, if even higher indium content epitaxial layers are to be grown, a simple approach of growing the layer directly on GaAs or on an intermediate SLS seems not to work as dislocations propagate from the interface through the epitaxial layer or are generated at the growing surface.

A novel approach to growing device-quality thick $\text{In}_{0.4}\text{Ga}_{0.6}\text{As}$ epitaxial layers on GaAs was developed in this work which involves the controlled propagation of dislocations via a carefully designed multi-stage strain-relief buffer system.

Cross-sectional and planar TEM analyses revealed the $\text{In}_{0.4}\text{Ga}_{0.6}\text{As}$ layers to have a low dislocation density ($10^6 - 10^7 \text{ cm}^{-2}$) in contrast to the heavily dislocated material obtained by growing $\text{In}_{0.4}\text{Ga}_{0.6}\text{As}$ directly on GaAs or using other structures to be described in this chapter. Hall-effect measurements performed on unintentionally doped $\text{In}_{0.4}\text{Ga}_{0.6}\text{As}$ indicated the room temperature electron concentrations in the epitaxial layer to be around $10^{15} - 10^{16} \text{ cm}^{-3}$ while electron mobilities were as high as $4,700 \text{ cm}^2 \text{ V}^{-1} \text{ sec}^{-1}$. Band-edge photoluminescence was recorded from these epilayers, the luminescence peak occurring at around 1,400 nm at room temperature and having a linewidth as small as 7 meV at 13 K.

In this chapter, the novel approach will be presented and discussed. Various steps taken during the development of the multi-stage strain-relief buffer system will also be discussed. In order to fully characterize the structures, cross-sectional and planar TEM, X-ray diffraction, photoluminescence, electron microprobe, and Hall-effect analyses are carried out on selected samples. A typical application for this buffered structure will be discussed.

Growth of High In Content $\text{In}_x\text{Ga}_{1-x}\text{As}$ Layers

In order to grow high indium content thick $\text{In}_x\text{Ga}_{1-x}\text{As}$ layers on GaAs substrates, an intermediate buffer system is necessary such that the misfit dislocations are kept confined at the interfaces or blocked from reaching the top epitaxial

layer of interest. The blocking role will be probably played by SLSSs since their stress fields tend to bend the dislocations towards the edges of the sample [59,60].

Utilization of a single strained-layer superlattice buffer having a suitable composition to make it lattice-matched to the InGaAs top layer proved not to work for high indium contents. A few different approaches were used to grow this kind of structure. The first one comprised the growth of an InGaAs/InAlAs superlattice with a relatively small difference between the lattice parameters of the two layers in order to eliminate the need to grow very thin layers. Very thin layers would be necessary to avoid reaching the critical thicknesses for each superlattice layer. If the individual layer thicknesses were larger than the critical value, the superlattice itself would be a source of dislocations. InAlAs layers were used due to practical limitations of the MBE system in growing alternate InGaAs layers with different indium contents since only a single indium source was available. Two structures were grown with one incorporating an InGaAs buffer layer before the superlattice. The second structure did not incorporate this buffer layer. Table 5.1 presents the various growth parameters for these two structures.

X-TEM analysis of these samples showed that the superlattice did not prevent dislocation propagation from the buffer layers through the InGaAs top layer.

Table 5.1 Growth parameters of two structures comprised of an InGaAs thick layer grown on an InGaAs/InAlAs SLS. In sample 037 the InGaAs buffer was not grown.

Sample	layers	n	x	thickness	GR (\AA sec^{-1})
036 & 037	InGaAs (top)	-	0.50	0.87 μm	4.48
	SLS: InAlAs	30	0.58	90 \AA	3.07
	" InGaAs	"	0.42	90 \AA	3.93
	InGaAs (buffer)	-	0.50	0.87 μm	4.48

The use of the InGaAs buffer did not improve the structure in any way, actually increasing the dislocation density in the superlattice and top layer. In the case of a sample without the intermediate InGaAs buffer, the superlattice showed a slight effect of blocking the dislocations originated at the GaAs/SLS interface but that was not sufficient to avoid propagation to the top layer. The presence of the InGaAs intermediate buffer seems to actually decrease the superlattice effectiveness because once the dislocations start propagating in a direction normal to the growth plane, they will have to find a sink to disappear and this is not the case when the InGaAs/SLS interface is reached. The two micrographs in Figure 5.1 illustrate the dislocation generation at the first heterointerface and their propagation all the way up into the InGaAs top layer.

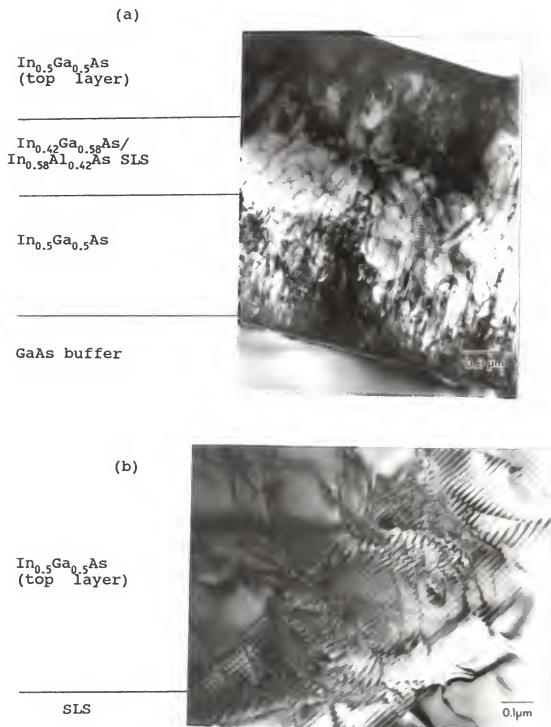


Figure 5.1 X-TEM micrographs of a structure composed of a $1.0\text{ }\mu\text{m}$ thick high indium content InGaAs layer grown on matched InGaAs/InAlAs SLS and InGaAs buffer layer showing (a) the whole structure and (b) a highly distorted SLS region.

Micrograph (a) shows the whole structure composed of an InGaAs buffer layer, an InGaAs/InAlAs SLS, and an InGaAs top layer. All three layers are assumed to be lattice-matched with respect to each other, but a large mismatch exists between the first InGaAs layer and the GaAs substrate ($\approx 3.5\%$). Micrograph (b) shows a detail of the SLS, which was so distorted that it is difficult to distinguish individual layers and their continuity. The micrograph in Figure 5.2

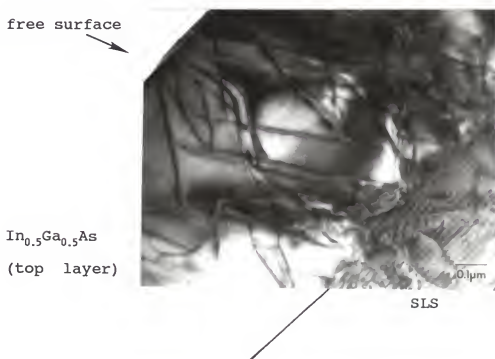


Figure 5.2 X-TEM micrograph of the top In_xGa_{1-x}As layer grown on a matched InGaAs/InAlAs SLS and InGaAs buffer layer.

illustrates the small reduction in dislocation density in the top layer if compared to the InGaAs buffer layer, indicating that even for those conditions, the SLS had some effect blocking a fraction of the dislocations. All three micrographs referred to above were taken from the same sample.

As a reduction in dislocation density was observed in the top InGaAs layer as compared to the InGaAs buffer layer, a structure similar to the two samples described above was grown with a double strained-layer superlattice with the same composition, number of periods, and layer thicknesses. Between these two layers, a 0.5 μm thick $\text{In}_{0.5}\text{Ga}_{0.5}\text{As}$ layer was introduced. This intermediate layer, as well as the InGaAs top layer were designed to be lattice-matched to the SLSs. X-TEM micrographs (a) and (b) of Figure 5.3 show a significant dislocation density reduction in the top layer when compared to the previous samples. Nevertheless, this dislocation density level is still too high if high-quality optoelectronic devices are to be built on such layers.

If strained-layer superlattices with larger compositional differences between the individual layers comprising the SLSs are grown, the individual layers must be kept thin since the critical thickness is decreased accordingly. This seems to reduce the superlattice efficacy in blocking the dislocations. In addition, a non-planar growth will be favored. The X-TEM micrographs of Figure 5.4 illustrate the effect of using superlattices with larger

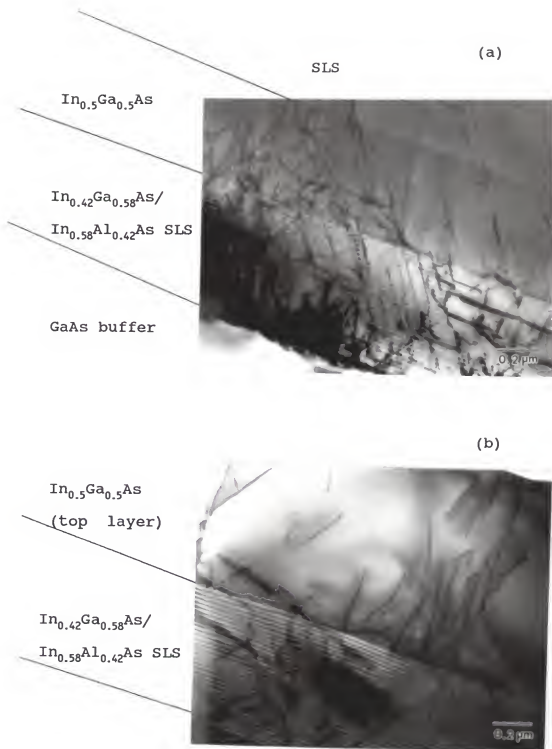


Figure 5.3 X-TEM micrographs of a structure with two InGaAs/InAlAs SLSS and an InGaAs layer grown between them: (a) the two SLSS and intermediate InGaAs layer; (b) top InGaAs layer showing a reduced dislocation density.

compositional difference. Micrograph (a) shows an $\text{In}_{0.35}\text{Ga}_{0.65}\text{As}/\text{In}_{0.65}\text{Al}_{0.35}\text{As}$ SLS with 60 periods and 50 Å thick layers grown directly on GaAs. An $\text{In}_{0.5}\text{Ga}_{0.5}\text{As}$ thick layer was grown after the superlattice. The superlattice layers are very dislocated and distorted, indicating a non-planar growth. A large amount of dislocations propagated through the InGaAs top layer. Micrograph (b) shows an extreme case: an $\text{In}_{0.5}\text{Ga}_{0.5}\text{As}$ top layer and an InAs/GaAs superlattice with 250 periods and ≈ 10 Å thick layers grown on GaAs. Due to the small thickness of the superlattice layers, they are not resolved for the magnification used in this picture but distortion similar to that observed in the previous sample could be expected as a spotty RHEED pattern was observed during growth of these structures indicating non-planar growth. Furthermore, it is clear that both superlattice and InGaAs top layer are heavily dislocated. In all samples where a high indium content SLS was grown, the GaAs buffer appeared to be dislocation-free. Figure 5.5 shows a X-TEM micrograph of a SLS grown directly on a GaAs buffer. The interface between the substrate and GaAs buffer layer is visible. It is evident that no dislocations propagated through the buffer and only some strain fields are observed close to the heterointerface. This result agrees with the findings in thick InGaAs/GaAs layers studied in chapter 4.

The approaches described above, used to grow high indium content InGaAs thick layers, did not work satisfactorily and the reason seems to be a lack of lattice-

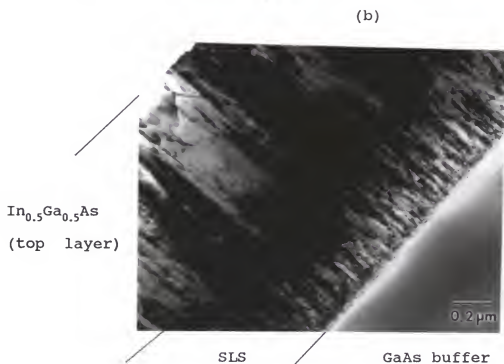
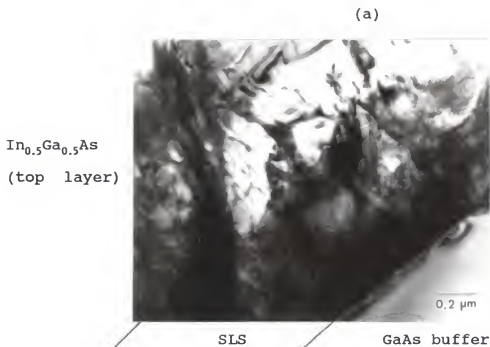


Figure 5.4 X-TEM micrographs of a 1.0 μm thick $\text{In}_{0.5}\text{Ga}_{0.5}\text{As}$ layer grown on different SLSs: (a) $\text{In}_{0.35}\text{Ga}_{0.65}\text{As}/\text{In}_{0.65}\text{Al}_{0.35}\text{As}$ SLS; (b) InAs/GaAs SLS.

matching of the whole structure to the substrate. If the superlattice is designed to be lattice-matched to the substrate, the superlattice layers will be alternately in biaxial compression and tension and as long as a critical

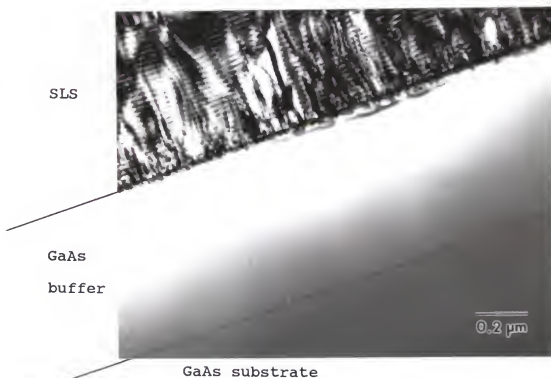


Figure 5.5 X-TEM micrograph of a sample showing the interface between the SLS and the GaAs buffer layer. No dislocations are observed in the buffer layer.

thickness is not exceeded for each individual layer, there is no limit for the total superlattice thickness. In the case where the superlattice is not lattice-matched to the substrate, its total thickness will be limited as it would be

for a single mismatched layer. The first misfit dislocations would appear at the interface with the substrate, a fraction of them propagating through the superlattice up into layers grown afterwards, and the rest suffering a bending action which would make them propagate in a direction perpendicular to the growth direction towards the edges of the substrate. In addition, when the lattice mismatch is large ($\approx 3\%$) as in the samples described above, where $\text{In}_x\text{Ga}_{1-x}\text{As}$ layers with $x \approx 0.5$ were pursued, the critical thickness approaches the size of the unit cell. At this point, it becomes difficult to obtain planar layers because 3-D growth is energetically favored [61] and a roughening of the growing surface occurs. This was observed clearly for all samples where a large mismatch was present in relation to the substrate. The 3-D growth mode does not help in any way the dislocation blocking action, because once the three-dimensional islands are formed at the growing surface, dislocation formation in the epitaxial layer is greatly favored.

Device-Quality $\text{In}_{0.4}\text{Ga}_{0.6}\text{As}$ Grown on GaAs

The phenomenon termed "critical composition" and described previously in chapter 4 was exploited in order to design a multi-stage strain-relief buffer system that ultimately would permit the growth of threading dislocation-free thick $\text{In}_{0.4}\text{Ga}_{0.6}\text{As}$ layers on GaAs. It was observed, as described earlier, that for values of x between zero and

approximately 0.16 for the alloy $\text{In}_x\text{Ga}_{1-x}\text{As}$, in addition to a high density of misfit dislocations confined at the $\text{In}_x\text{Ga}_{1-x}\text{As}/\text{GaAs}$ interface, strain due to lattice-mismatch is partially relieved by plastic deformation of the GaAs substrate material with the $\text{In}_x\text{Ga}_{1-x}\text{As}$ epitaxial layers remaining essentially dislocation-free. Threading dislocations propagate in the GaAs material on account of its lower bulk shear modulus.

A complex structure composed of various stages, each one comprising an InGaAs buffer layer and a strained-layer superlattice, was realized to take advantage of the strain relief process which was expected to occur by steps at the interfaces between the SLSs of suitable composition and the buffer layers in such a way that misfit dislocations would thread only into these underlying buffers [62]. A group of four samples was grown according to the schematic diagram shown in Figure 5.6, with the $\text{In}_{0.4}\text{Ga}_{0.4}\text{As}$ top layer grown at different temperatures, namely 400, 427, 453, and 480°C, all other growth conditions remaining the same for this set of samples. In order to assure the compositional difference (Δx) would not exceed the critical value of ≈ 0.16 , Δx was made ≈ 0.14 for each stage. This value should be the largest possible, without reaching the critical Δx , in order to reduce the number of stages necessary to grow high x top $\text{In}_x\text{Ga}_{1-x}\text{As}$ layers (in this study, $x \approx 0.4$).

As can be seen from the diagram, the "first stage" of the multi-stage buffer system consisted of a 0.2 μm thick

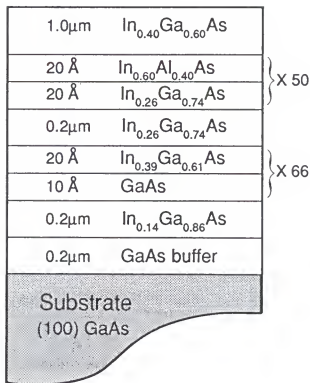


Figure 5.6 Schematic diagram of a "multi-stage" strain-relief buffer system grown by MBE in order to realize device-quality $\text{In}_{0.4}\text{Ga}_{0.6}\text{As}$ epilayers on GaAs.

$\text{In}_{0.14}\text{Ga}_{0.86}\text{As}$ layer grown on GaAs which was designed to relieve stress in the system developed to this point in the manner discussed above. The subsequent strain-relieving stages incorporated in the buffer system were designed in such a way as to promote dislocation propagation primarily in underlying

"sacrificial" layers, namely the 0.2 μm thick $\text{In}_{0.14}\text{Ga}_{0.86}\text{As}$ and the 0.2 μm thick $\text{In}_{0.26}\text{Ga}_{0.74}\text{As}$ epitaxial layers.

In order to grow the multi-stage strain-relief buffer structure, a number of growth interruptions were necessary, which consisted of shuttering of the group III element fluxes while maintaining an As_2 flux. These interruptions were necessary to permit a change in either the substrate temperature or in the group III flux levels such that particular ternary alloy compositions could be achieved. The GaAs buffer layer was grown at 600°C and following a growth interruption, the $\text{In}_{0.14}\text{Ga}_{0.86}\text{As}$ layer was grown at 520°C. Following a second interruption, the first strained-layer superlattice was grown at 480°C as was the $\text{In}_{0.26}\text{Ga}_{0.74}\text{As}$ layer. Growth was again interrupted such that the second strained-layer superlattice could be grown at 440°C and finally both substrate temperature and element fluxes were adjusted in order to grow the thick $\text{In}_{0.4}\text{Ga}_{0.6}\text{As}$ layer. Layer growth rates varied throughout the structure depending on the total group III element flux levels, ranging from 2.8 Å/s for the InAlAs layers to 6.5 Å/s for the top InGaAs layer.

Cross-sectional TEM analysis performed on the multi-stage buffer system confirmed the designed stress-relief pattern. As can be seen from Figure 5.7 (a) and (b), a dramatic reduction in the density of threading dislocations observed in cross-section is achieved by employing the multi-stage strain-relief system when compared to the situation with

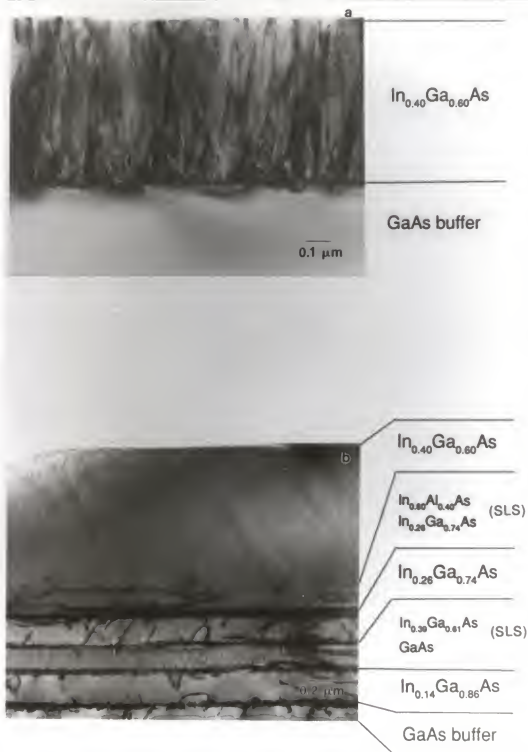


Figure 5.7 X-TEM micrographs illustrating (a) heavily dislocated $\text{In}_{0.4}\text{Ga}_{0.6}\text{As}$ grown directly on GaAs and (b) nearly dislocation-free $\text{In}_{0.4}\text{Ga}_{0.6}\text{As}$.

respect to direct growth of $\text{In}_{0.4}\text{Ga}_{0.6}\text{As}$ layers on GaAs, which represents close to a 3% lattice-mismatched system. As indicated in Figure 5.7 (b), the top InGaAs layer, which in this case is 1 μm thick, appears, in fact, to be threading dislocation-free. A relatively low dislocation density was later calculated to be around 10^8 cm^{-2} in this set of samples by counting dislocation lines in planar TEM in the same manner as described in chapter 4. The strain-relief process in the multi-stage system is quite evident by inspection of the TEM micrograph shown in Figure 5.7 (b). Non-lateral threading dislocations appear to propagate in the "sacrificial" layers, namely the GaAs buffer, the $\text{In}_{0.14}\text{Ga}_{0.86}\text{As}$ and the $\text{In}_{0.26}\text{Ga}_{0.74}\text{As}$ layers, while the few dislocations observed in the two SLSs appear to propagate laterally. The SLSs are not resolved under the diffraction conditions which are optimum for dislocation observation, namely, two beam, $g = \langle 220 \rangle$ reflection, however, the individual layers comprising the two SLSs are clearly illustrated in Figure 5.8 employing a two beam, $g = \langle 400 \rangle$ reflection condition.

The device-quality nature of $\text{In}_{0.4}\text{Ga}_{0.6}\text{As}$ epitaxial layers grown at different temperatures with such multi-stage buffers incorporated was confirmed by Hall-effect measurements and photoluminescence (PL) analysis. Data obtained with these analyses in a number of samples are presented in Table 5.2, which, in addition, includes the results obtained from composition analysis performed with an electron microprobe and

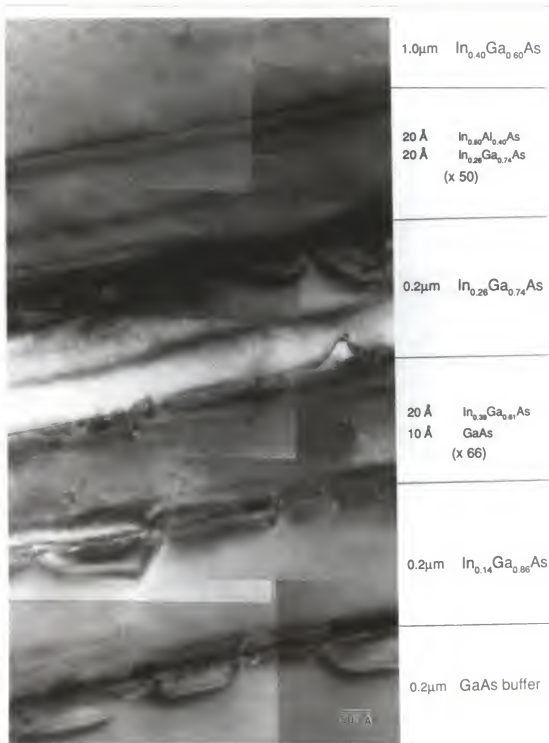


Figure 5.8 X-TEM micrograph composite of the complete "multi-stage" buffer system illustrating the strained-layer superlattices.

Table 5.2 Experimental data of thick $\text{In}_{0.4}\text{Ga}_{0.6}\text{As}$ layers grown on GaAs.

Samples →		071	062	069	070
T_{ss} (top layer) (°C)		400	427	453	480
effective strain (%)		0.22	-	-	0.43
alloy composition (x)		0.39	0.40	-	0.39
carrier concentr. n (cm^{-3})		2.0 E15	5.6 E14	2.7 E15	4.7 E15
Hall mobility μ ($\text{cm}^2 \text{V}^{-1} \text{s}^{-1}$)		3371	2922	2361	1749
dislocation density ρ (cm^{-2})		-	10^8	10^8	10^8
PL	wavelength $\lambda(300\text{K})$ (nm)	-	-	1.416	1.368
	wavelength $\lambda(13\text{K})$ (nm)	-	-	1.334	1.265
	linewidth 13K (meV)	-	-	42.6	16.5
	intensity 13K (a.u.)	-	-	160	360

effective strain calculated from X-ray diffraction spectra.

Hall-effect measurements performed at room temperature on unintentionally-doped InGaAs layers revealed the free electron densities to be in the range from $\approx 6 \times 10^{14}$ to $5 \times 10^{15} \text{ cm}^{-3}$ for this set of samples, with electron mobilities

ranging from ≈ 1750 to $3400 \text{ cm}^2 \text{ V}^{-1} \text{ s}^{-1}$. Since only substrate temperature during growth of the InGaAs top layer changed in this group of samples, the growth conditions otherwise constant, the dependence of electron mobility on substrate temperature was obtained, the lower the temperature, the higher the mobility.

Photoluminescence analysis was performed at room temperature and 13K on the buffered epitaxial layers. The apparatus included an Argon-ion laser with $\lambda = 5145 \text{ \AA}$, power output = 30 mW, and spot diameter $\approx 200 \text{ }\mu\text{m}$, an Instruments S.A. monochromator, a liquid nitrogen cooled Ge photodiode detector, and an EG&G analyzer operating in a lock-type mode. It is seen that for this particular composition, the PL peaks occurred at $\approx 1.4 \text{ }\mu\text{m}$ at room temperature and $1.3 \text{ }\mu\text{m}$ at 13K. Those values can change significantly if strain is present in the epitaxial layer.

In a sample where composition was measured in the top $\text{In}_{0.4}\text{Ga}_{0.6}\text{As}$ layer by electron microprobe, x being 0.39, a comparison can be made to the band gap values obtained from works of different authors, Adachi [58] and Nahory et al. [55]. According to these two works, the expected wavelengths for unstrained material should be 1375 nm and 1369 nm, respectively, at room temperature. The PL wavelength peak for this sample was found to be 1368 nm, in excellent agreement with the expected values for unstrained materials. Due to the lack of data for 13K, a direct comparison was impossible, but

comparison to the expected value for 2K [58], 1274 nm, shows that a good agreement seemed to occur since the measured value for 13K was 1265 nm.

These results indicate that the $\text{In}_{0.4}\text{Ga}_{0.6}\text{As}$ layer was essentially strain-free. Nevertheless, X-ray diffraction analysis of the top layer showed there was some remaining strain in the top layer. The effective strain presented in Table 5.2 was calculated differently than the residual strains discussed in chapter 4 for single layers grown directly on GaAs. In the present case, there was no data about the underlying SLS lattice parameter so that the residual strain could not be calculated. Thus, an "effective" strain was adopted to describe the strain state in the top layer, being defined as

$$\text{effective strain (\%)} = \frac{a_{\text{meas}} - a_r}{a_r} \times 100, \quad (5.1)$$

where a_{meas} is the measured value from the X-ray diffraction spectrum and a_r is the lattice parameter of the unstrained (bulk) InGaAs, as defined in chapter 4.

At this point, it was quite evident that the basic process, by which threading dislocations were blocked from propagating to the top InGaAs layer, was working satisfactorily. Nevertheless, some improvements could be possible by investigating the new pieces of information obtained from the various analysis techniques. Some

adjustments in composition of the superlattice layers and intermediate buffer layers were made to assure a closer lattice-matching between the SLSs and layers grown afterwards.

Two structures were grown with the objective of investigating the effect of different SLS designs on the top layer quality and studying the structure's ability to work satisfactorily for other indium contents in the top InGaAs layer. The first structure (# 068) was grown in a similar way as the samples in the group described above, but the top $\text{In}_{0.4}\text{Ga}_{0.6}\text{As}$ had its thickness reduced to $0.2\ \mu\text{m}$ and an additional $\text{In}_{0.7}\text{Al}_{0.3}\text{As}/\text{In}_{0.36}\text{Ga}_{0.64}\text{As}$ strained-layer superlattice with 50 periods and $20\ \text{\AA}$ thick layers was grown, followed by a $1\ \mu\text{m}$ thick $\text{In}_{0.53}\text{Ga}_{0.47}\text{As}$ layer, both grown at 440°C . The second structure (# 072) was grown with a different composition in the last SLS, namely $\text{In}_{0.66}\text{Al}_{0.34}\text{As}/\text{In}_{0.4}\text{Ga}_{0.6}\text{As}$, all other growth conditions remaining the same. This last design modification permitted to eliminate the growth interruption necessary to change the $\text{In}_x\text{Ga}_{1-x}\text{As}$ composition from $x = 0.40$ to 0.36 and also led to a reduction in the compositional difference (Δx) of the last SLS from 0.34 to 0.26 . Furthermore, it changed the strain state in this superlattice from biaxial tensile stress in the InGaAs layers and biaxial compressive stress in the InAlAs layers to theoretically zero stresses in the InGaAs layers and lower levels of biaxial compressive stresses in the InAlAs layers with regard to the underlying InGaAs buffer layer.

Hall-effect measurements performed at room temperature indicated the electron concentration to be 1.6×10^{16} and $1.5 \times 10^{16} \text{ cm}^{-3}$, while a dramatic increase in electron mobility occurred, the values being 1018 and $4020 \text{ cm}^2 \text{ V}^{-1} \text{ s}^{-1}$, respectively, for the first (# 068) and second (# 072) structures. Planar TEM of sample # 072 revealed a dislocation density equal to $2 \times 10^8 \text{ cm}^{-2}$. No planar TEM was performed on sample # 068 but a much higher dislocation density was observed in XTEM analysis of this sample when compared to the second structure (# 072).

Photoluminescence analysis at room temperature and 13K of sample # 072 confirmed the previous good results, with a intense luminescence peak at 1622 and 1574 nm, respectively, at room temperature and 13K. The linewidth at 13K was measured to be 11 meV. The peak wavelength at room temperature compares fairly well to the expected values cited in the works discussed above [55,58], which give, respectively, 1663 and 1649 nm for $\text{In}_{0.53}\text{Ga}_{0.47}\text{As}$ unstrained layers with the small difference due probably to a slightly composition deviation from the expected value.

The TEM and Hall-effect measurements indicate that the SLS design was critical for obtaining appropriate material properties, the main factor being either the compositional difference between SL layers or the stress state in both layers. In addition, these results showed that the multi-stage

strain-relief system approach was useful when top InGaAs layers with different compositions were desired.

To investigate which factor was dominant in the improvement observed in structure # 072, a structure (# 073) was grown under similar conditions of group # 062 - # 071 (Figure 5.6), the differences being the following: (i) the second buffer composition was increased slightly from $x = 0.26$ to 0.27 ; (b) the second superlattice remained with one layer, $\text{In}_{0.27}\text{Ga}_{0.73}\text{As}$, with the same compositions of the underlying InGaAs buffer and the other SL layer composition was changed from $x = 0.60$ to 0.53 , in such a way that the SL average lattice parameter would match the top $\text{In}_{0.4}\text{Ga}_{0.6}\text{As}$ layer parameter; (c) as a consequence, the compositional difference in this last superlattice was reduced from 0.34 to 0.26 . Thus, if these modifications are compared to the changes imposed on sample # 072, it is observed that only Δx was reduced (by the same amount), but no stress state changes in the SLS were expected. The substrate temperature was kept at 400°C during growth of the top InGaAs layer, a temperature which led to the best carrier mobilities, measured in structure # 071.

Hall-effect measurements revealed no significant improvements in electron mobilities, which changed from 3371 to $3398 \text{ cm}^2 \text{ V}^{-1} \text{ s}^{-1}$. Hence, the compositional difference in the SLS layers seems not to be critical to the properties of layers grown afterwards with the main role probably due to the stress state in the SLS.

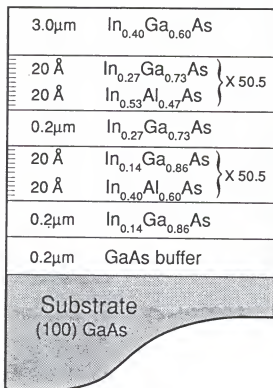


Figure 5.9 Schematic diagram of a "multi-stage" strain-relief system with a slightly different SLS design

Further structures (# 074, 076, 077, 079, and 082) were designed in order to take advantage of the last improvements. As can be seen from the schematic diagram in Figure 5.9, the first superlattice was modified to have its InGaAs layer composition equal to the first InGaAs buffer layer such that it would not be strained with regard to this buffer. The $\text{In}_x\text{Al}_{1-x}\text{As}$ SL layer composition was changed to $x =$

0.40 to make the SLS average lattice parameter equal to the next $\text{In}_{0.27}\text{Ga}_{0.73}\text{As}$ buffer parameter. The second SLS and top layer compositions remained the same as in structure # 073. The only difference between structures # 074 and 076 was the As_2 beam flux. This flux was changed so that the $\text{BEP}(\text{As}_2):\text{BEP}(\text{Ga}+\text{In})$, beam equivalent pressure ratio between arsenic and metals, was dropped from 21.1 to 6.4 during growth of the top InGaAs layer to determine the role of this parameter in the electronic properties of that epitaxial layer. The results obtained from Hall-effect measurements, X-ray diffraction, electron microprobe, and photoluminescence analysis are listed in Table 5.3, for this group of structures. Structure # 077 had its top InGaAs layer grown at 370°C , with an intermediate BEP ratio equal to 10.9, while the top InGaAs layer of structure # 079 was grown at 350°C with the same flux ratio. During the growth of structure # 082, a lower flux ratio was used to compare its properties to structure # 079.

All samples of this group consistently presented higher electron mobilities and lower dislocation densities than the samples of the previous group, indicating a clear improvement in the top epitaxial layer quality when the new SLS design was employed. Figure 5.10 shows typical planar TEM micrographs of samples which presented different dislocation density. Micrograph (a) shows a region of a sample where a few threading dislocations are observed reaching the free surface of the top $\text{In}_{0.4}\text{Ga}_{0.6}\text{As}$. This sample presented an overall

Table 5.3 Experimental data obtained from thick $\text{In}_{0.4}\text{Ga}_{0.6}\text{As}$ epitaxial layers grown on a multi-stage strain-relief buffer.

Samples →		074	076	077	079	082	088
T_{ss} (°C)		400	400	370	350	350	370
BEP (As/M) ratio		21.1	6.4	10.9	10.5	5.4	9.1
eff. strain (%)		0.19	0.12	0.15	0.29	-	-
composition (x)		0.41	0.41	0.41	0.41	0.42	0.37
n (cm ⁻³)		4.2 E15	1.3 E15	9.1 E15	4.3 E16	4.7 E16	3.4 E16
μ (cm ² V ⁻¹ s ⁻¹)		3766	3808	4671	4302	4364	3604
ρ (cm ⁻²)		8 E6	4 E6	2 E6	6 E6	2 E7	5 E6
PL	λ (300K) (nm)	1.427	1.435	1.396	1.412	-	-
	λ (13K) (nm)	1.320	1.385	1.304	1.305	-	-
	lw 13K (meV)	16.4	54.0	7.0	9.2	-	-
	Int. 13K (a.u.)	920	100	865	680	-	-

dislocation density of $\approx 10^8 \text{ cm}^{-2}$. Micrograph (b) shows the top surface of a sample with a dislocation density equal to $2 \times 10^6 \text{ cm}^{-2}$, i.e., close to the detection limit of the technique

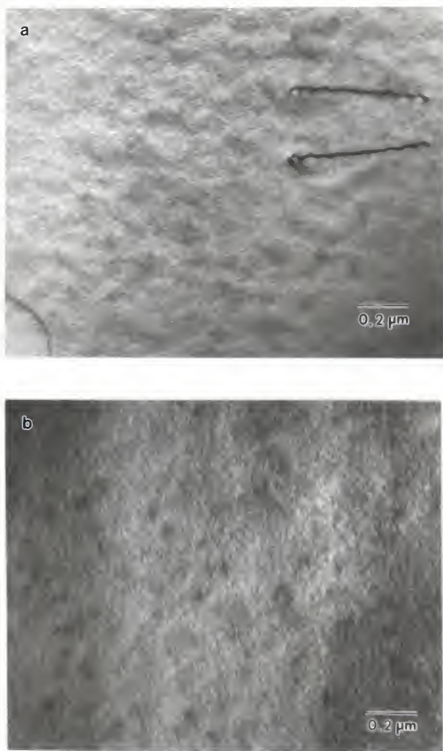


Figure 5.10 Planar TEM micrographs of two samples presenting dislocation densities equal to (a) $\approx 10^8 \text{ cm}^{-2}$ and (b) $\approx 2 \times 10^6 \text{ cm}^{-2}$, respectively.

employed. In this last sample, only a few dislocations could be counted over all regions analyzed.

Photoluminescence characteristics also showed some improvement with respect to linewidth and peak intensity, the best sample presenting a peak linewidth at half height as low as 7.0 meV. A typical PL spectrum is presented in Figure 5.11.

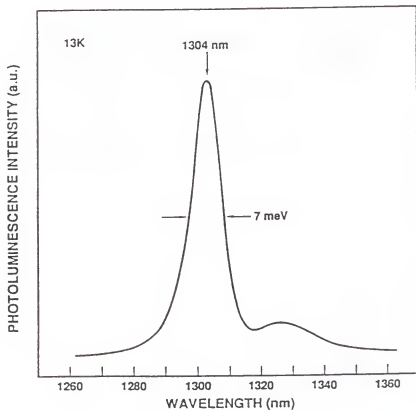


Figure 5.11 Typical 13K photoluminescence spectrum recorded from a 3 μm thick buffered $\text{In}_{0.4}\text{Ga}_{0.6}\text{As}$ epitaxial layer grown on GaAs.

The rather narrow linewidth of the luminescence peak shown in this figure, i.e., 7 meV, is only a factor of two greater than that recorded from lattice-matched $\text{In}_{0.53}\text{Ga}_{0.47}\text{As}$ epitaxial layers grown on InP by metal-organic chemical vapor deposition. The peak wavelengths remained nearly constant at 1.4 μm . The small variations observed for layers of nearly the same composition may be due to small fluctuations in composition from region to region in the same sample or slightly different strain state, both difficult to evaluate with the available analysis methods.

$\text{In}_{0.4}\text{Ga}_{0.6}\text{As}$ carrier mobilities proved not to be sensitive to the $\text{BEP}(\text{As}_2):\text{BEP}(\text{In}+\text{Ga})$ ratio in the range listed in Table 5.3. Nevertheless, for a ratio as low as 2.6, a surface roughening and poor material properties indicated the As_2 flux was not sufficient to maintain an arsenic-stabilized surface. Therefore, a minimum $\text{BEP}(\text{As}_2):\text{BEP}(\text{In}+\text{Ga})$ ratio of ≈ 6 should be maintained for the substrate temperature and composition ranges employed in this work.

Lowering substrate temperature to 370°C during growth of the top InGaAs led to higher mobilities and better PL characteristics, namely peak linewidth and intensity. For even lower substrate temperatures (350°C), no further benefits could be observed. In fact, the electron mobility decreased slightly from 4,670 to 4,300 $\text{cm}^2 \text{V}^{-1} \text{s}^{-1}$ and dislocation density increased from 2×10^6 to $6 \times 10^6 \text{ cm}^{-2}$, when the substrate temperature changed from 370°C to 350°C (structures # 077 and

079), the growth conditions otherwise the same. Furthermore, the PL peak linewidth at 13K increased from 7 to 9.2 meV and absolute peak intensity decreased.

Finally, a structure (# 088) was grown using a different design for the SLSs in such a way that both individual layers comprising the SL would be in biaxial compressive stress with regard to the underlying InGaAs buffer layer. This design would complete the range of possibilities for the stress state of the SLSs so that a whole picture would be obtained for the strain relief process. The two SLSs were composed of $\text{In}_{0.2}\text{Ga}_{0.8}\text{As}/\text{In}_{0.34}\text{Al}_{0.66}\text{As}$ and $\text{In}_{0.33}\text{Ga}_{0.67}\text{As}/\text{In}_{0.47}\text{Al}_{0.53}\text{As}$ layers with the same number of periods (50) and layer thickness (20 Å) of the last group of structures. The substrate was kept at 370°C during growth of the top InGaAs layer and $\text{As}_2:(\text{In}+\text{Ga})$ flux ratio was 9.1 so that a direct comparison to structure # 077 was possible.

A significant decrease in electron mobility was observed when this last SLS design was employed although dislocation density did not show a large variation between these two structures (# 077 and 088). The carrier mobility seems to be a better method to assess material quality because it covers a larger area. The method employed for measuring dislocation density offers a good estimate of the real value but considers only a very small area of a sample. Thus, it is very sensitive to small variations of strain or composition which may occur from region to region in a same structure. At

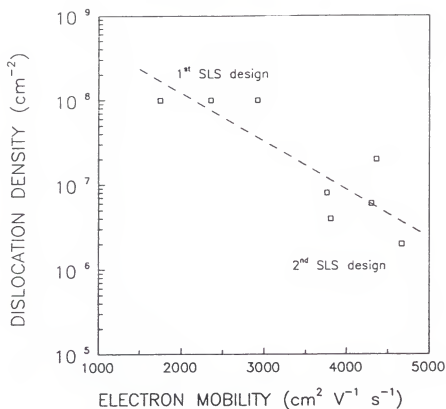


Figure 5.12 Dislocation density versus electron mobility in buffered In_{0.4}Ga_{0.4}As epitaxial layers grown on GaAs.

the other extreme, Hall-effect gives an average value of a property measured over a much larger area, i.e., about 6 x 6 mm, of each structure, therefore being a more accurate indication of material quality, as far as electronic properties are concerned.

Nevertheless, dislocation density was also a useful tool principally in those cases where systematic variation

occurred. For instance, if a comparison is made between the two last groups of structures, listed in Table 5.2 and Table 5.3, a reduction of 1 to 2 orders of magnitude, on average, is observed when the second type of SLS design is employed.

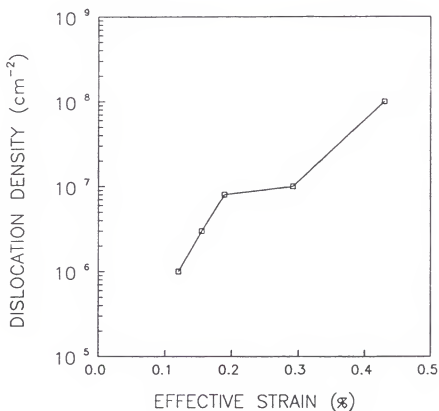


Figure 5.13 Dislocation density as a function of effective strain in buffered $\text{In}_{0.4}\text{Ga}_{0.6}\text{As}$ epitaxial layers grown on GaAs.

The graphics presented in Figure 5.12 and Figure 5.13 plot dislocation density versus electron mobility and effective strain, respectively. It is observed that a reasonable relationship occurs in both cases indicating that dislocation density appears to be a function of effective strain, the higher the strain, the more dislocated the epitaxial layer will be. Furthermore, higher carrier mobilities are obtained in more perfect layers.

In_{0.4}Ga_{0.6}As p-i-n Photodetector Fabrication

It was pointed out that a strong motivation for this work was to produce In_xGa_{1-x}As photonic devices operating in the 1.0 - 1.7 μm wavelength range which could be grown on GaAs substrates, such that they could be incorporated in GaAs ICs. The utilization of the multi-stage buffer subject of the present work permitted the successful fabrication for the first time of a high quality In_{0.4}Ga_{0.6}As/GaAs p-i-n photodiode with a peak photoresponse at 1.3 μm [63].

Since such devices require doped layers, two 3 μm thick In_{0.4}Ga_{0.6}As layers were grown on the multi-stage buffer, to determine the carrier concentration as a function of dopant (both n- and p-type) source temperatures. The results are presented in Table 5.4. It was found that these results are comparable to the carrier concentrations and mobilities obtained in GaAs layers, thus a linear relationship was

assumed to occur when different doping levels were pursued, in the same manner as described for GaAs in chapter 3.

Table 5.4 Electronic properties of doped $\text{In}_{0.4}\text{Ga}_{0.6}\text{As}$ layers obtained by Hall-effect measurements at room temperature.

Source temperature (°C)	Dopant	Mobility ($\text{cm}^2\text{V}^{-1}\text{s}^{-1}$)	Carrier concentrat. (cm^{-3})	Resistivity ($\Omega\text{ cm}$)
1310	Si	2010	3.9 E18	8.1 E-4
900	Be	56	4.9 E18	2.3 E-2

The photodetector structure reported here and presented schematically in Figure 5.14 has completely eliminated the need for incorporating phosphorus in the active layer. The device comprises a $0.4\text{ }\mu\text{m}$ thick $\text{p}^+\text{-In}_{0.4}\text{Ga}_{0.6}\text{As}$ layer, a $0.8\text{ }\mu\text{m}$ thick undoped $\text{In}_{0.4}\text{Ga}_{0.6}\text{As}$ layer, and a $0.3\text{ }\mu\text{m}$ thick $\text{n}^+\text{-In}_{0.4}\text{Ga}_{0.6}\text{As}$ layer grown on top of the strain-relieved undoped $\text{In}_{0.4}\text{Ga}_{0.6}\text{As}$ layer.

C-V measurements of the undoped $\text{In}_{0.4}\text{Ga}_{0.6}\text{As}$ revealed an unintentional doping concentration of $3.5 \times 10^{15}\text{ cm}^{-3}$, consistent with the previous Hall-effect measurements in the top $\text{In}_{0.4}\text{Ga}_{0.6}\text{As}$ [63].

The spectral response of the photodetector is shown in Figure 5.15. The photoresponse peak corresponds to a wavelength of $1.3\text{ }\mu\text{m}$ with a responsivity equal to 0.45 A/W and

polyimide or other dielectrics [63]. A cutoff wavelength of $\approx 1.4 \mu\text{m}$ is observed which is consistent with PL and absorption measurements performed in layers with the same indium content.

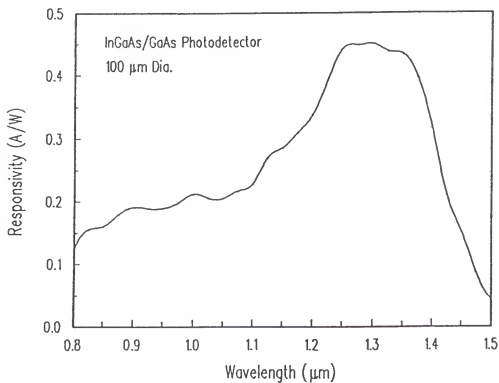


Figure 5.15 Spectral response of an $\text{In}_{0.4}\text{Ga}_{0.6}\text{As}$ p-i-n photodiode prepared on a GaAs substrate.

Conclusions

A multi-stage strain-relief buffer system was realized so that high-quality $\text{In}_x\text{Ga}_{1-x}\text{As}$ with high indium contents could be grown on GaAs substrates. A comparison to InGaAs layers with the same composition grown directly on GaAs or on a single stage buffer system showed that a dramatic improvement in material properties was obtained in the case of the incorporation of the multi-stage system. Lower dislocation densities, higher electron mobilities, and better photoluminescence characteristics were consistently found in those layers grown on the multi-stage buffer system.

It was possible to determine the stress state in strained-layer superlattice individual layers which leads to the best material properties by comparing these properties for different SLS designs. It was found that the approach which presented the best results involved alternate layers subjected to respectively no stresses and biaxial compressive stresses with regard to the underlying InGaAs buffer. In other words, the SL InGaAs layer should have the same composition of the previous InGaAs buffer layer while the InAlAs presented a higher indium content. The subsequent InGaAs buffer layer should be lattice-matched to the SLS in such a way that no stresses would be generated at the interface between these two layers. This approach seemed to increase the SLS efficacy in

blocking dislocations from propagating through subsequent layers.

A p-i-n photodetector prepared in $\text{In}_{0.4}\text{Ga}_{0.6}\text{As}$ layers grown on top of the multi-stage buffer structure discussed in this chapter, operated well at the $1.3\text{ }\mu\text{m}$ wavelength, showing a very good responsivity (around 0.45 A/W) and quantum efficiency (42%). This demonstrates the feasibility of this multi-stage "strain-relief" buffer system for the fabrication of optoelectronic devices operating in the important near-IR wavelength regime (1.0 to $1.7\text{ }\mu\text{m}$). This would make possible lasers and detectors operating in this wavelength range to be monolithically integrated with highly developed GaAs integrated circuits.

CHAPTER 6

CONCLUSIONS AND RECOMMENDATIONS

The $\text{In}_x\text{Ga}_{1-x}\text{As}/\text{GaAs}$ system was studied for a wide range of compositions. It was demonstrated during the course of this investigation that, in spite of the lattice mismatch between the $\text{In}_x\text{Ga}_{1-x}\text{As}$ and GaAs compounds, it is possible to grow a variety of structures in such a way that the layer of interest presents a low dislocation density, comparable to the initial dislocation density of the substrates.

For $\text{In}_x\text{Ga}_{1-x}\text{As}$ with low indium content ($x < 0.16$), it was found that thick layers can be grown directly on GaAs, the misfit dislocations being confined to the $\text{In}_x\text{Ga}_{1-x}\text{As}/\text{GaAs}$ interface with some propagating into the GaAs buffer layer. The dislocation density in this case is lower than the limit of the measurement technique employed ($2 \times 10^5 \text{ cm}^{-2}$). The critical composition was defined as the composition value above which dislocations nucleate at the epilayer free surface. This composition was found to be between $x = 0.16$ and 0.18 for $\text{In}_x\text{Ga}_{1-x}\text{As}$ epitaxial layers.

Growth of higher indium content ($x > 0.3$) $\text{In}_x\text{Ga}_{1-x}\text{As}$ directly on GaAs results in heavily dislocated epitaxial layers. If an $\text{In}_x\text{Ga}_{1-x}\text{As}/\text{GaAs}$ SLS is introduced between the

substrate and the $\text{In}_x\text{Ga}_{1-x}\text{As}$ layer, its average lattice parameter being equal to the corresponding $\text{In}_x\text{Ga}_{1-x}\text{As}$ parameter, dislocations generated at the GaAs/SLS interface propagate into the SLS and finally reach the $\text{In}_x\text{Ga}_{1-x}\text{As}$ top layer. Thus, a different approach is required to grow high quality $\text{In}_x\text{Ga}_{1-x}\text{As}$ layers on GaAs substrates.

A novel approach designed to reduce significantly the dislocation density in high indium content $\text{In}_x\text{Ga}_{1-x}\text{As}$ epitaxial layers was developed in this work. This approach involved the controlled propagation of dislocations via a multi-stage strain-relief buffer system where the dislocations appear to propagate in the "sacrificial" layers, namely the GaAs buffer and the $\text{In}_x\text{Ga}_{1-x}\text{As}$ layers of intermediate composition, while the few dislocations observed in the SLSs propagate laterally towards the edges of the samples.

A particular alloy composition, $x = 0.4$, was chosen in this work in order to demonstrate the feasibility of the technique. However, it is believed that high-quality $\text{In}_x\text{Ga}_{1-x}\text{As}$ epitaxial layers could be grown on GaAs by suitable selection of the stage materials, in order to provide material for optoelectronic device operation at other important wavelengths, for example, $1.55 \mu\text{m}$ ($\text{In}_{0.48}\text{Ga}_{0.52}\text{As}$).

The efficacy of this novel approach was evident in the successful fabrication for the first time of a low dark current and high sensitivity planar $\text{In}_{0.4}\text{Ga}_{0.6}\text{As}$ p-i-n photodetector presenting a quantum efficiency of 42% and a

responsivity of 0.45 A/W at 1.3 μm , using GaAs as a substrate and the multi-stage strain-relief system as an intermediate buffer.

It is believed that the primary objective of this study has been fulfilled although it is possible that not all growth conditions or intermediate stage compositions are optimized.

Further developments of this multi-stage system could include use of $\text{In}_x\text{Ga}_{1-x}\text{As}/\text{In}_y\text{Ga}_{1-y}\text{As}$ SLSs instead of $\text{In}_x\text{Ga}_{1-x}\text{As}/\text{In}_y\text{Al}_{1-y}\text{As}$ SLSs in the final stage of the buffer. It is expected that the use of only $\text{In}_x\text{Ga}_{1-x}\text{As}$ compounds could lead to a better composition control, hence SLS average lattice parameter control. A slight deviation from the desired lattice parameter value could originate strain in the top $\text{In}_x\text{Ga}_{1-x}\text{As}$ layer, so that significant modifications in the material properties would result. Furthermore, if only $\text{In}_x\text{Ga}_{1-x}\text{As}/\text{In}_y\text{Ga}_{1-y}\text{As}$ compounds are used, composition deviations will be absorbed equally by all layers, thus if there is a shift in the lattice parameter, this will occur for the whole structure. Therefore, an easier lattice matching between the SLSs and subsequent layers would be obtained, although a change in the blocking behavior is a possibility if $\text{In}_y\text{Al}_{1-y}\text{As}$ is replaced by $\text{In}_y\text{Ga}_{1-y}\text{As}$.

An improvement for this multi-stage structure would be the utilization of a double SLS with the same composition, as the last step before the final and top $\text{In}_x\text{Ga}_{1-x}\text{As}$ layer is grown. An intermediate $\text{In}_x\text{Ga}_{1-x}\text{As}$ layer should be grown between

them, with the same composition as the top $\text{In}_x\text{Ga}_{1-x}\text{As}$ layer. Since it is observed that a few dislocations manage to reach the top $\text{In}_x\text{Ga}_{1-x}\text{As}$ layer, it is expected that the last SLS would block most of those defects in such a way that they would be confined to the intermediate $\text{In}_x\text{Ga}_{1-x}\text{As}$ layer of same composition.

For future experimental work, the development of a multi-stage system designed to work with higher indium content $\text{In}_x\text{Ga}_{1-x}\text{As}$ layers is suggested. It is indicated in the present study that such an approach works satisfactorily for x as high as 0.55, which corresponds to a wavelength of $\approx 1.70 \mu\text{m}$ at room temperature.

REFERENCES

1. W. T. Tsang, in **Semiconductors and Semimetals** (R. K. Williardon and A. C. Beer, ed.), vol. 22, Part A, Academic, New York, 1985, p. 95.
2. I. J. Fritz, L. R. Dawson, and T. E. Zipperian, *J. Vac. Sci. Technol. B* **1**, 387 (1983).
3. B. I. Miller, J. H. McFee, R. J. Martin, and P. K. Tien, *Appl. Phys. Lett.* **33**, 44 (1978).
4. S. Arai and Y. Suematsu, *IEEE J. Quantum Electron.*, **QE-16**, 197 (1980).
5. G. L. Olsen and M. E. Henberg, in **Crystal Growth** (C. H. L. Goodman, ed.), vol. 2, Plenum, New York, 1978, p. 1.
6. W. T. Tsang, F. K. Reinhart, and J. A. Ditzenberger, *Appl. Phys. Lett.* **41**, 1094 (1982).
7. G.D. Holah, F. L. Eisele, E. L. Meeks, and N. W. Cox, *Appl. Phys. Lett.* **41**, 1073 (1982).
8. D. M. Collins, in **Frontiers in Electronic Materials and Processing** (L. J. Brillson, ed.), AIP, New York, 1985, p. 208.
9. A. Y. Cho, *Thin Solid Films* **100**, 291 (1983).
10. W. D. Laidig, C. K. Peng, and Y. F. Lin, *J. Vac. Sci. Technol. B* **2**, 181 (1984).
11. C. E. Barnes, G. A. Samara, R. M. Biefeld, T. E. Ziperian, and G. C. Osbourn, *Proc. of 13th Intern. Conf. on Defects in Semiconductors* (L. C. Kimerling and J. M. Parsley Jr., ed.), AIME Pub., New York, 1985, p. 471.
12. K. H. Chang, P. K. Bhattacharya, and R. Gibala, *J. Appl. Phys.* **65**, 3391 (1989).
13. J. H. van der Merwe and W. A. Jesser, *J. Appl. Phys.* **63**, 1510 (1988).

14. W. A. Jesser and J. H. van der Merwe, *J. Appl. Phys.* **63**, 1928 (1988).
15. P. M. Petroff, in *Semiconductors and Semimetals* (R. K. Williardon and A. C. Beer, ed.), vol. 22, Part A, Academic, New York, 1985, p. 379.
16. J. W. Matthews and A. E. Blakeslee, *J. Cryst. Growth* **27**, 118 (1974).
17. G. M. Olsen and M. Ettenberg, *Crystal Growth Theory and Tech.* **2**, 15 (1978).
18. E. A. Fitzgerald, P. D. Kirchner, R. Proano, G. D. Pettit, J. M. Woodall, and D. G. Ast, *Appl. Phys. Lett.* **52**, 1496 (1988).
19. W. Hagen and H. Strunk, *Appl. Phys. Lett.* **17**, 86 (1978).
20. C. Herbeaux, J. Di Persio, and F. Lefebvre, *Appl. Phys. Lett.* **54**, 1004 (1989).
21. E. A. Fitzgerald, D. G. Ast, Y. Ashizawa, S. Akbar, and L. F. Eastman, *J. Appl. Phys.* **64**, 2473 (1988).
22. J. W. Matthews, S. Mader, and T. B. Light, *J. Appl. Phys.* **41**, 3800 (1970).
23. H. Nakao and T. Yao, *Jpn. J. Appl. Phys.* **28**, L352 (1989).
24. J. H. van der Merwe, *J. Appl. Phys.* **34**, 123 (1962).
25. R. People and J. C. Bean, *Appl. Phys. Lett.* **47**, 322 (1985).
26. J. W. Matthews and A. E. Blakeslee, *J. Cryst. Growth* **27**, 118 (1974).
27. P. J. Orders and B. F. Usher, *Appl. Phys. Lett.* **50**, 980 (1987).
28. I. J. Fritz, P. L. Gourley, and L. R. Dawson, *Appl. Phys. Lett.* **51**, 1004 (1987).
29. G. C. Osbourn, *J. Appl. Phys.* **53**, 1586 (1982).
30. G. C. Osbourn, *J. Vac. Sci. Technol.* **21**, 469 (1982).
31. G. C. Osbourn, *Phys. Rev. B* **27**, 5126 (1983).

32. P. M. J. Marée, J. C. Barbour, J. F. van der Veen, K. L. Kavanagh, C. W. T. Bulle-Lieuwma, and M. P. A. Vieggers, *J. Appl. Phys.* **62**, 4413 (1987).
33. M. Gal, P. C. Taylor, B. F. Usher, and P. J. Orders, *J. Appl. Phys.* **62**, 3898 (1987).
34. F. J. Grunthaner and A. Madhukar, *J. Vac. Sci. Technol. B* **1**, 462 (1983).
35. L. F. Eastman, *J. Vac. Sci. Technol. B* **1**, 131 (1983).
36. A. Chin, P. Bhattacharya, W-P. Hong, and W-Q Li, *J. Vac. Sci. Technol. B* **6**, 665 (1988).
37. C. E. C. Wood, in *GaInAsP Alloy Semiconductors* (T. P. Pearsall, ed.), Wiley, New York, 1982, p. 87.
38. D. C. Radulescu, W. J. Schaff, L. F. Eastman, J. M. Ballingall, G. O. Ramseyer, and S. D. Hersee, *J. Vac. Sci. Technol. B* **7**, 111 (1989).
39. E. G. Scott, D. A. Andrews, and G. J. Davies, *J. Vac. Sci. Technol. B* **4**, 534 (1986).
40. P. R. Berger, K. Chang, P. Bhattacharya, J. Singh, and K. K. Bajaj, *Appl. Phys. Lett.* **53**, 684 (1988).
41. G. L. Price, *Appl. Phys. Lett.* **53**, 1288 (1988).
42. S. V. Ghaisas and A. Madhukar, *Appl. Phys. Lett.* **53**, 1599 (1988).
43. L. B. Loeb, in *The Kinetic Theory of Gases*, 3rd ed., Dover Publications, New York, 1961, p. 19.
44. D. M. Collins, Corporate Research Memorandum CRM-346, Varian Associates, Santa Clara, May 1979.
45. S. Ingrey, W. M. Lau, and N. S. McIntyre, *J. Vac. Sci. Technol. A* **4**, 984 (1986).
46. C. F. Yu, M. T. Schmidt, D. V. Podlesnik, E. S. Yang, and R. M. Osgood Jr., *J. Vac. Sci. Technol. A* **6**, 754 (1988).
47. A. Y. Cho, *J. Appl. Phys.* **41**, 2780 (1970).
48. A. Y. Cho, *J. Vac. Sci. Technol.* **8** (5), s31 (1971).
49. J. S. Blakemore, *J. Appl. Phys.* **53**, R123 (1982).

50. J. K. Abrokwhah, N. C. Cirillo Jr., M. J. Helix, and M. Longerbone, *J. Vac. Sci. Technol. B* **2**, 252 (1984).
51. T. J. Drummond, W. G. Lyons, R. Fisher, R. E. Thorne, and H. Morkoc, *J. Vac. Sci. Technol.* **21** (4), 957 (1982).
52. D. M. Collins, D. E. Mars, and S. J. Eglash, *J. Vac. Sci. Technol. B* **1**, 170 (1983).
53. P. D. Kirchner, J. M. Woodall, J. L. Freeauf, D. J. Wolford, and G. D. Pettit, *J. Vac. Sci. Technol.* **19**, 604 (1981).
54. L. G. Salmon and I. J. D'Haenens, *J. Vac. Sci. Technol. B* **2**, 197 (1984).
55. R. E. Nahory, M. A. Pollack, W. D. Johnston Jr., and R. L. Barns, *Appl. Phys. Lett.* **33**, 659 (1978).
56. K. L. Kavanagh, M. A. Capano, L.W. Hobbs, J. C. Barbour, P. M. J. Maree, W. Schaff, J. W. Mayer, D. Pettit, J. M. Woodall, J. A. Stroschio, and R. M. Feenstra, *J. Appl. Phys.* **64**, 4843 (1988).
57. H. C. Casey Jr., A. Y. Cho, and P. A. Barnes, *IEEE J. Quantum Electron.* **11**, 467 (1975).
58. S. Adachi, *J. Appl. Phys.* **53**, 8775 (1982).
59. N. A. El-Masry, J. C. Tarn, and N. H. Karam, *J. Appl. Phys.* **64**, 3672 (1988).
60. Z. J. Radzinski, B. L. Jiang, G. A. Rozgonyi, T. P. Humphreys, N. Hamaguchi, C. Parker, and S. M. Bedair, *Appl. Phys. Lett.* **52**, 1692 (1988).
61. J. Y. Marzin and J. M. Gerard, *Superl. and Microst.* **5**, 51 (1989).
62. P. Ribas, V. Krishnamoorthy, and R. M. Park, manuscript accepted, *Appl. Phys. Lett.* (1990).
63. S. S. Li, Y. C. Tzeng, Y. W. Lin, P. Ribas, and R. M. Park, manuscript submitted for publication (Jul 1990).

BIOGRAPHICAL SKETCH

Paulo Roberto Fogaça Ribas was born on August 17, 1949, in Santa Maria, RS, Brazil. He is married to Marcia Virginia L. Ribas, and has three sons, Rafael, 16, Gabriel, 16, and Renato, 12, and one daughter, Priscilla Maria, 9.

He joined the Brazilian Army in 1968 enrolling in the Military Academy of Agulhas Negras as a cadet. He graduated in 1971 and was commissioned as a lieutenant in the Army Ordnance Corps.

In 1977, he entered the Military Institute of Engineering, located in Rio de Janeiro, and received the bachelor's degree in metallurgical engineering in 1979. After finishing his bachelor's degree, he was commissioned as an engineer in the Military Engineer Corps and transferred to the Third Military Region Command, in Porto Alegre, RS, where he worked for two years. In 1982, he was invited to be an instructor at the Military Academy of Agulhas Negras, where he taught undergraduate courses for three years.

He started his master's degree program in 1985, at the Military Institute of Engineering, defending his thesis on "Preparation and Characterization of $\text{CuInSe}_2/\text{CdS}$ Solar Cells" in February of 1987.


After receiving his master's degree in materials science, he was selected by the Brazilian Army to pursue doctoral studies in the Department of Materials Science and Engineering of the University of Florida, enrolling in this institution in the Spring of 1988.

I certify that I have read this study and that in my opinion it conforms to acceptable standards of scholarly presentation and is fully adequate, in scope and quality, as a dissertation for the degree of Doctor of Philosophy.



Robert M. Park, Chairman
Associate Professor of Materials
Science and Engineering

I certify that I have read this study and that in my opinion it conforms to acceptable standards of scholarly presentation and is fully adequate, in scope and quality, as a dissertation for the degree of Doctor of Philosophy.



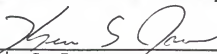
Paul H. Holloway
Professor of Materials Science and
Engineering

I certify that I have read this study and that in my opinion it conforms to acceptable standards of scholarly presentation and is fully adequate, in scope and quality, as a dissertation for the degree of Doctor of Philosophy.



Rolf E. Hummel
Professor of Materials Science and
Engineering

I certify that I have read this study and that in my opinion it conforms to acceptable standards of scholarly presentation and is fully adequate, in scope and quality, as a dissertation for the degree of Doctor of Philosophy.



Kevin S. Jones
Assistant Professor of Materials
Science and Engineering

I certify that I have read this study and that in my opinion it conforms to acceptable standards of scholarly presentation and is fully adequate, in scope and quality, as a dissertation for the degree of Doctor of Philosophy.



Sheng S. Li
Professor of Electrical Engineering

This dissertation was submitted to the Graduate Faculty of the College of Engineering and to the Graduate School and was accepted as partial fulfillment of the requirements for the degree of Doctor of Philosophy.

August 1990



for Winfred M. Phillips
Dean, College of Engineering



Madelyn M. Lockhart
Dean, Graduate School